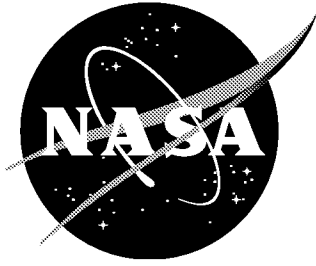


NASA / TP-2001-210839



# Structure-Property Correlations in Al-Li Alloy Integrally Stiffened Extrusions

*Stephen J. Hales and Robert A. Hafley  
Langley Research Center, Hampton, Virginia*

---

April 2001

## The NASA STI Program Office ... in Profile

Since its founding, NASA has been dedicated to the advancement of aeronautics and space science. The NASA Scientific and Technical Information (STI) Program Office plays a key part in helping NASA maintain this important role.

The NASA STI Program Office is operated by Langley Research Center, the lead center for NASA's scientific and technical information. The NASA STI Program Office provides access to the NASA STI Database, the largest collection of aeronautical and space science STI in the world. The Program Office is also NASA's institutional mechanism for disseminating the results of its research and development activities. These results are published by NASA in the NASA STI Report Series, which includes the following report types:

- **TECHNICAL PUBLICATION.** Reports of completed research or a major significant phase of research that present the results of NASA programs and include extensive data or theoretical analysis. Includes compilations of significant scientific and technical data and information deemed to be of continuing reference value. NASA counterpart of peer-reviewed formal professional papers, but having less stringent limitations on manuscript length and extent of graphic presentations.
- **TECHNICAL MEMORANDUM.** Scientific and technical findings that are preliminary or of specialized interest, e.g., quick release reports, working papers, and bibliographies that contain minimal annotation. Does not contain extensive analysis.
- **CONTRACTOR REPORT.** Scientific and technical findings by NASA-sponsored contractors and grantees.

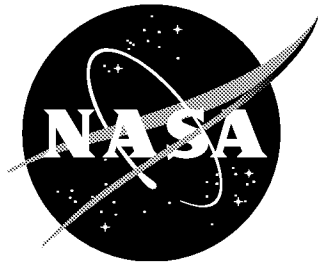
- **CONFERENCE PUBLICATION.** Collected papers from scientific and technical conferences, symposia, seminars, or other meetings sponsored or co-sponsored by NASA.
- **SPECIAL PUBLICATION.** Scientific, technical, or historical information from NASA programs, projects, and missions, often concerned with subjects having substantial public interest.
- **TECHNICAL TRANSLATION.** English-language translations of foreign scientific and technical material pertinent to NASA's mission.

Specialized services that complement the STI Program Office's diverse offerings include creating custom thesauri, building customized databases, organizing and publishing research results ... even providing videos.

For more information about the NASA STI Program Office, see the following:

- Access the NASA STI Program Home Page at <http://www.sti.nasa.gov>
- E-mail your question via the Internet to [help@sti.nasa.gov](mailto:help@sti.nasa.gov)
- Fax your question to the NASA STI Help Desk at (301) 621-0134
- Phone the NASA STI Help Desk at (301) 621-0390
- Write to:  
NASA STI Help Desk  
NASA Center for Aerospace Information  
7121 Standard Drive  
Hanover, MD 21076-1320

NASA/TP-2001-210839



# Structure-Property Correlations in Al-Li Alloy Integrally Stiffened Extrusions

*Stephen J. Hales and Robert A. Hafley  
Langley Research Center, Hampton, Virginia*

National Aeronautics and  
Space Administration

Langley Research Center  
Hampton, Virginia 23681-2199

---

April 2001

The use of trademarks or names of manufacturers in the report is for accurate reporting and does not constitute an official endorsement, either expressed or implied, of such products or manufacturers by the National Aeronautics and Space Administration.

---

Available from:

NASA Center for AeroSpace Information (CASI)  
7121 Standard Drive  
Hanover, MD 21076-1320  
(301) 621-0390

National Technical Information Service (NTIS)  
5285 Port Royal Road  
Springfield, VA 22161-2171  
(703) 605-6000

## CONTENTS

LIST OF FIGURES .....	iv
LIST OF TABLES.....	v
Abstract .....	1
1. Introduction.....	1
2. Experimental Procedures .....	3
3. Results and Discussion .....	6
3.1 Texture.....	6
3.2 Grain Structure.....	8
3.3 Tensile Properties.....	9
3.4 Fracture Toughness Properties.....	10
3.5 Texture-Yield Strength Correlations .....	11
4. Concluding Remarks .....	15
5. Acknowledgements .....	16
6. References.....	16
7. Appendix.....	40

## LIST OF FIGURES

Figure 1.	Taylor-type models, ranked by decreasing levels of constraint from the Taylor model, through various Relaxed Constraint models, to the Sachs model, where $\epsilon_{xy}$ refers to shear on the plane perpendicular to the X direction in the Y direction and $\epsilon_{cc}$ is the Poisson effect .....	20
Figure 2.	Photographs of the extrusions.....	21
Figure 3.	Extrusion schematic showing cross-sectional geometry, dimensions and nomenclature adopted; (A)xial, (R)adial, (C)ircumferential. ....	22
Figure 4.	3-D schematic of texture fibers, using Bunge notation[26], illustrating the relative positions of common {hkl} and <uvw>fibers found in Al alloys in Euler space. ....	23
Figure 5.	Typical ODF data, all $\phi_2$ sections. ....	24
Figure 6.	Mechanical test specimen schematic, showing the location and orientation of specimens machined from the extrusions in the Skin and Base regions. ....	25
Figure 7.	2195 texture characteristics. ....	26
Figure 8.	2098 texture characteristics. ....	27
Figure 9.	2096 texture characteristics. ....	28
Figure 10.	2195 macrostructural characteristics; Nomarski contrast images; R-C plane; Skin and Base regions.....	29
Figure 11.	2098 macrostructural characteristics; Nomarski contrast images; R-C plane; Skin and Base regions.....	30
Figure 12.	2096 macrostructural characteristics; Nomarski contrast images; R-C plane; Skin and Base regions.....	31
Figure 13.	2195 microstructural and microtextural characteristics at t/2.....	32
Figure 14.	2098 microstructural and microtextural characteristics at t/2.....	33
Figure 15.	2096 microstructural and microtextural characteristics at t/2.....	34
Figure 16.	2195 mechanical properties in Skin and Base, data includes range bars.....	35
Figure 17.	2098 mechanical properties in Skin and Base, data includes range bars.....	36
Figure 18.	2096 mechanical properties in Skin and Base, data includes range bars.....	37
Figure 19.	Taylor Factor calculations: full constraint (F) vs. relaxed constraint (IGD) models; -90° to +90° orientation. ....	38
Figure 20.	Normalized Taylor factor ( $\bar{M}/3.06$ ) vs. normalized yield strength ( $\sigma_{ys}/\sigma_{ys}(0)$ ) for Full constraint (F) vs. Relaxed constraint (IGD) models. ....	39
Figure A1.	Mechanical behavior of 2195 Skin. Stress-strain curves and K-R curves for various orientations. ....	41
Figure A2.	Mechanical behavior of 2195 Base. Stress-strain curves and K-R curves for various orientations. ....	42
Figure A3.	Mechanical behavior of 2098 Skin. Stress-strain curves and K-R curves for various orientations. ....	43
Figure A4.	Mechanical behavior of 2098 Base. Stress-strain curves and K-R curves for various orientations. ....	44
Figure A5.	Mechanical behavior of 2096 Skin. Stress-strain curves and K-R curves for various orientations. ....	45
Figure A6.	Mechanical behavior of 2096 Base. Stress-strain curves and K-R curves for various orientations. ....	46

## LIST OF TABLES

Table 1. Alloy Compositions.....	3
Table 2. Alloy Processing .....	3
Table 3. Common Texture Components in Al Alloys .....	5
Table 4. Average Tensile and Toughness Properties .....	10
Table 5. Texture Characteristics @ t/2 vs. Yield Strength Anisotropy .....	12
Table 6. Texture/Anisotropy Rankings .....	13

## Abstract

*Aluminum-lithium near-net-shape extrusions are viable candidates for structural applications on a variety of aerospace vehicles. The objective of this investigation was to establish the relationship between mechanical property anisotropy, microstructure and crystallographic texture in integrally 'T'-stiffened extruded panels fabricated from alloys 2195, 2098 and 2096. In-plane properties were measured as a function of orientation with respect to the extrusion direction at two representative locations in the panels, namely mid-way between (Skin), and directly beneath (Base), the integral 'T' stiffeners. The 2195 extrusion exhibited the best combination of strength and toughness, but was the most anisotropic. The 2098 extrusion exhibited lower strength and comparable toughness, but was more isotropic than 2195. The 2096 extrusion exhibited the lowest strength and poor toughness, but was the most isotropic. All three alloys exhibited highly elongated grain structures and similar location-dependent variations in grain morphology. The textural characteristics comprised a  $\beta + \langle 100 \rangle$  fiber texture, similar to rolled product, in the Skin regions and a  $\langle 111 \rangle + \langle 100 \rangle$  fiber texture, comparable to axisymmetric extruded product, in the Base regions. In an attempt to quantitatively correlate texture with yield strength anisotropy, the original 'full constraint' model, pioneered by Taylor, and a variant of the 'relaxed constraint' model, explored by Wert and co-workers, were applied to the data. A comparison of the results revealed that the Wert model was consistently more accurate than the Taylor model. Discrepancies between the predictions and the measured yield strength anisotropy were addressed in terms of the heterogeneous microstructural and textural characteristics observed.*

## 1. Introduction

Opportunities to use near-net-shape extrusions for aerospace structural applications, where eliminating joints and fasteners is beneficial, are being explored [1, 2]. The use of reduced density aluminum-lithium (Al-Li) alloys in combination with lower part count is expected to be economical as a result of lower structural weight and simplified manufacturing operations [3]. However, the mechanical property anisotropy of extruded products with complex cross-sections, resulting from heterogeneous material flow during the extrusion process, has tended to jeopardize widespread application. This effect is compounded by the fact that Li-bearing Al alloys, regardless of product form, typically exhibit unrecrystallized grain structures with strong textures and through-thickness gradients which culminate in highly anisotropic behavior [4]. Considerable research has been conducted on structure/property relationships in Al-Li rolled products [5-8], but previous work on Al-Li extrusions has tended to concentrate on processing/property [9-12] and processing/structure [13, 14] relationships, rather than establishing quantitative structure/property correlations per se [15, 16]. A survey of the literature also revealed that information concerning the behavior of extrusions with the complex cross-sectional geometries typically required for structural applications is sparse. Consequently, improved methods which can predict mechanical anisotropy based on microstructural and/or textural characteristics in these types of engineering materials need to reach maturation.

Research on Al alloys has shown that mechanical anisotropy is governed primarily by crystallographic texture, with grain morphology and coherent precipitate effects playing secondary roles [8, 17-19]. Models developed to correlate texture with mechanical behavior assume that a polycrystalline material can be described as an aggregate of single crystal grains with different crystallographic orientations [20-22]. The basic premise is that there is no interaction between grains and the behavior of the aggregate is determined by the collective behavior of the individual grains. The yielding of individual grains is considered to be solely dependent on orientation with respect to the tensile axis and the imposed strain state [23]. In complex-textured materials, the relative volume fractions of grains with specific crystallographic orientations can be quantified by employing orientation distribution function (ODF) analysis [24, 25]. Consequently, the yield strength anisotropy exhibited by extruded materials can be



predicted via Taylor-type relationships [15, 16]. Existing models, formulated to relate textural characteristics to yield strength anisotropy, can be broadly categorized by the degree of constraint employed [26]. Constraint refers to the number of independent active slip systems in each grain that are considered necessary to support deformation of a polycrystalline aggregate under a specified strain state. In Al alloys (f.c.c.), there are 12 operable slip systems of the type  $\{111\}\langle 110\rangle$ , capable of imparting strain to each grain, but only five systems need to be activated to retain material contiguity [23, 26].

The various models which have been proposed are ranked in terms of the degree of constraint in Figure 1, which also illustrates the difference in the associated grain shape changes [23, 26]. The Full constraint (F) model, proposed by Taylor, allows 5 active slip systems in each grain and allows no shear deformation on any of the principal specimen planes [21, 22]. The relationship takes the form:

$$\sigma_{ys} = \bar{M} \cdot \tau_{CRSS}$$

where  $\sigma_{ys}$  is the yield strength of the aggregate,  $\tau_{CRSS}$  is the critical resolved shear stress for a single crystal and  $\bar{M}$  is the average Taylor factor. In contrast, the No constraint (N) model, proposed by Sachs, allows only 1 active slip system in each grain and shear deformation on all three specimen planes and also allows for the Poisson effect [20]. This relationship takes the form:

$$\sigma_{ys} = (1/\bar{m}) \cdot \tau_{CRSS}$$

where  $\bar{m}$  is the average Schmid factor. Relaxed constraint (R) models reside in-between the Taylor and Sachs models by allowing plastic deformation to be imparted by the activation of 2, 3 or 4 slip systems in each grain. Reduction in the number of slip systems responsible for overall specimen deformation can be brought about by elongated grain morphologies, in concert with specific textural compositions [23]. For a material comprising randomly oriented grains, it is generally accepted that  $\bar{M}= 3.06$  and  $1/\bar{m}= 2.24$  [20, 21, 26]. Therefore, the fewer slip systems that are active, the lower is the yield strength predicted assuming a constant value for the critical resolved shear stress of a single crystal. Consequently, the F and N models form the upper and lower bounds, respectively, for yield strength predictions, with R-type models providing intermediate values.

In this study, refinements to the R-type models proposed by Wert et al. for precipitation-strengthened materials are explored. The Wert ‘plastic inclusion’ model assumes that non-axisymmetric strain states are allowed and that each grain can undergo a different shape change than the aggregate [27-29]. Specifically, the ‘independent grain deformation’ (IGD) variant of the Wert model applied in this work still treats each grain in the aggregate as a separate entity and allows it to deform independently of its neighbors. The key assumption of the IGD model is that individual grains adopt the strain state which minimizes the yield strength of that grain for each strain axis orientation and the number of active slip systems is not specified [30, 31]. The model works by an iterative process which steps through the various R-type models (as illustrated in Figure 1) in order to compute the minimum yield strength. By permitting non-axisymmetric strain states within grains, the predicted stress at which the aggregate deforms as a whole will always be lower than that predicted by the F model. In previous work, predictions by the IGD model suggest that the contribution of precipitates to plastic anisotropy is of secondary importance compared to that of crystallographic texture [31]. Hence, the role of precipitates in explaining orientation-dependent yield strength variations was not included in the present work. The objectives of this investigation were: (i) to compare and contrast the mechanical anisotropy exhibited by the three extrusions; (ii) to study the relationships between microstructural / textural characteristics and tensile / toughness properties; and (iii) to evaluate the F and IGD model outputs for predicting yield strength anisotropy based on quantitative texture analyses.

## 2. Experimental Procedures

The Al-Li near-net-shape extrusions studied in this investigation were produced at Wyman Gordon (Houston, TX) from ingots produced by Reynolds Metals Company (McCook, IL). The compositions of the 2195, 2098 (formerly RX818) and 2096 ingots are shown in Table 1, and details of the processing, which have been outlined previously, are summarized in Table 2 [32]. The extrusions were produced as 33 in. internal diameter cylinders with the T stiffeners located on the outer surface, Figure 2(a). The final lengths of the extrusions were 255 in. for 2195, 120 in. for 2098 and 165 in. for 2096. These were then split length-wise, flattened, solution heat treated, stretched, naturally aged and artificially aged to a T8 temper condition, Figure 2(b). The major difference between the alloy compositions is the variation in the Cu:Li ratio which governs the solution and aging heat treatments (temperature and time) required to achieve the T8 temper condition. The alloys were designed by Reynolds to reside in a common phase field, such that the Cu:Li ratio merely affects the primary precipitate volume fraction and the maximum attainable strength level [33]. The varying Cu:Li ratio (and total solute content) was manifested in subtle differences in the effective homologous temperature ( $T/T_M$  in K) for both hot working, due to the common extrusion temperature, and the solution heat treatment/aging temperatures selected for each alloy.

Table 1. Alloy Compositions

Alloy	Nominal Elemental Composition (wt. pct.)					
	Cu	Li	Mg	Ag	Zr	Al
2195	4.05	1.05	0.46	0.44	0.14	Bal.
2098	3.62	0.91	0.48	0.38	0.15	Bal.
2096	2.38	1.42	0.73	0.31	0.14	Bal.

Figure 3 shows details of the cross-sectional geometry of the extruded panels and outlines the nomenclature adopted to describe the locations and orientations within the extrusions. Considering differential material flow during the extrusion process, two representative locations were identified for study. These locations are the skin mid-way between the stiffeners and the skin at the base of the stiffeners, which will hereafter be referred to as the ‘Skin’ and ‘Base’ regions in discussion. (Note that the vertical portion of the T stiffener is referred to as the ‘Web’ and the horizontal segment, as the ‘Cap’). The Base region is of interest because of the microstructural and textural heterogeneities introduced during the extrusion process and the localized effect on mechanical properties. In contrast to rolled product, through-thickness locations in the extruded product were not expected to be symmetrical about the mid-plane [34-36]. Therefore, the depth locations are defined from  $t_o$  (the *outer* surface) through  $t/4$ ,  $t/2$  (the mid-plane) and  $3t/4$  to  $t_i$  (the *inner* surface) of the cylindrical cross-section (with the ‘T’ stiffeners being located on the outer surface). Mechanical test specimen orientations were defined with respect to the principal axes of the original cylindrical extruded cross-section. The (A)xial direction is parallel to

Table 2. Alloy Processing

Alloy	Extrusion		Solution Heat Treat.		Stretch, %	T8 Aging Treatment	
	Temp., °F	Ratio	Temp., °F	Time, hrs		Temp., °F	Time, hrs
2195	750	18:1	950	1	3.4	300	20
2098	750	18:1	980	1	1.6	310	24
2096	750	18:1	980	1	2.8	330	30

the extrusion direction, the (C)ircumferential direction is perpendicular to the extrusion direction in the plane of the skin and the (R)adial direction is perpendicular to both the extrusion direction and the plane of the skin.

Metallographic examination of the Skin and Base regions was conducted through thickness for macrostructural studies and centered at  $t/2$  for microstructural evaluation. Nomarski contrast of Keller's etched specimens was used to reveal material flow lines in the macroscopic images and cross-polarized illumination of anodized specimens was used to reveal grain contrast in the optical micrographs. Crystallographic x-ray data for the Skin and Base regions at the  $t_0$ ,  $t/4$ ,  $t/2$ ,  $3t/4$  and  $t_i$  locations were collected with a Philips x-ray diffractometer using  $\text{CuK}\alpha$  radiation with tube settings of 40kV and 30mA. Since a 0.75 in. square texture sample was required and the stiffener width was only 0.125 in., a laminate consisting of six 0.75 in. long sections from the same stiffener was assembled for collecting Base region data. The raw data were corrected with respect to background intensity and defocusing errors using data collected from a randomly-textured pure Al powder specimen. Quantitative texture analysis involved measuring three incomplete (111), (200) and (220) pole figures from which ODF's were calculated via the series expansion method using commercial software [24]. Through-thickness variations in texture intensities were determined by plotting orientation density,  $f(g)$ , along recognized texture fibers in Euler space (employing the Bunge notation, i.e.  $\phi_1, \phi, \phi_2$ ) [24, 25, 37].

Figure 4 illustrates the main texture fibers frequently associated with Al alloy products which were considered in this study [26]. Selected other texture components common in Al alloys, but not contained within these fibers, were also included in the analyses [24, 25, 38-41]. All of the deformation-related (DF-) and recrystallization-related (RX-) components used to establish textural characteristics are listed in Table 3. The relative intensities of these fibers and components were determined from ODF plots such as those shown in Figure 5 for the 2098 extrusion in the Skin and Base regions. The complete  $\phi_2$  sections shown essentially represent a 2-D rendition of Euler space. The 'box' presentation of Euler space in Figure 4 has been adjusted relative to the ODF data in Figure 5 such that the continuous nature of the fibers can best be envisioned. Comparing Figure 4 with Figure 5;  $\phi_2 = 0^\circ$  to  $45^\circ$  (ODF) corresponds to  $\phi_2 = 0^\circ$  to  $45^\circ$  (box), while  $\phi_2 = 45^\circ$  to  $90^\circ$  (ODF) corresponds to  $\phi_2 = -45^\circ$  to  $0^\circ$  (box). Particularly significant to this work are the  $\beta$  (rolling) and  $\langle 111 \rangle$  (extrusion) fibers which start together at the Cu orientation (@  $\phi_2 = -45^\circ$ ) in the schematic and extend through Euler space with a  $\phi_1$  separation of  $15\text{-}20^\circ$  [14, 42]. Similar texture components contained within these rolling- and extrusion-related deformation fibers are: S related to  $\text{Ex}_2$  (@  $\phi_2 = -35^\circ$ ), Brass to  $\text{Ex}_1$  (@  $\phi_2 = 0^\circ$ ) and  $\text{S}'_1$  to  $\text{Ex}_3$  (@  $\phi_2 = 20^\circ$ ). The offset between these fibers ( $\phi_1 = 15\text{-}20^\circ$ ) can also be observed by comparing the typical data contained in Figures 5(a) & 5(b).

The specimen layout for mechanical testing is outlined in Figure 6; tensile properties were determined in  $15^\circ$  increments to the extrusion direction and fracture toughness properties at  $0^\circ$  (L-T),  $45^\circ$  (45-45) and  $90^\circ$  (T-L) only. Tensile tests were conducted using sub-size flat specimens with gage dimensions of 1 in. long x 0.25 in. wide x 0.15 in. thick, in conformance with ASTM E8 [43]. Duplicate tests were performed at a constant cross head speed of 0.01 in./min. in a servo-hydraulic test frame. Strain-to-failure was measured using back-to-back extensometers. Duplicate fracture toughness tests were conducted using compact tension (C(T)) specimens with  $W = 2$  in. and  $B = 0.15$  in. conforming with ASTM E813 and E1152 [44,45]. The C(T) specimens for the Base regions were extracted such that the end of the fatigue pre-crack was centered beneath the stiffener. Physical crack lengths were determined using DC potential drop methods. The resulting J-R curves were converted to K-R curves using the relationship:

$$K = [(J \cdot E) / ((1 - \nu^2))]^{1/2}$$

where  $E$  is Young's modulus and  $\nu$  is Poisson's ratio [46]. Initiation toughness ( $K_{I0}$ ), defined as the toughness at 0.004 in. stable crack extension, was determined from K-R curves using prescribed methods [46,47]. It is important to note that the thickness of the tensile and C(T) specimens, centered on  $t/2$ , extended from approximately  $t/4$  to  $3t/4$  in the extruded cross-sections.

Table 3. Common Texture Components in Al Alloys

Type	Component	{hkl}<uvw>	Euler Angles (Bunge)		
			$\phi_1$	$\phi$	$\phi_2$
Deformation:	Bs	{011}<211>	35	45	0
	S	{123}<634>	55	35	65
	S' <sub>1</sub>	{123}<412>	25	60	20
	S' <sub>2</sub>	{146}<211>	55	85	35
	Cu	{112}<111>	90	30	45
	Ex <sub>1</sub>	{011}<111>	50	45	0
	Ex <sub>2</sub>	{123}<111>	75	35	65
	Ex <sub>3</sub>	{134}<111>	40	60	20
	Shear <sub>1</sub>	{001}<110>	0	0	45
	Shear <sub>2</sub>	{111}<110>	0	55	45
	Shear <sub>3</sub>	{112}<110>	0	35	45
Recrystallization:	Goss	{011}<100>	0	45	0
	Cube	{001}<100>	0	0	0
	RC <sub>RD1</sub>	{013}<100>	0	20	0
	RC <sub>RD2</sub>	{023}<100>	0	35	0
	RC <sub>ND1</sub>	{001}<310>	20	0	0
	RC <sub>ND2</sub>	{001}<320>	35	0	0
	P	{011}<122>	70	45	0
	Q	{013}<231>	55	20	0
	R	{124}<211>	55	75	25
	Bs <sub>RX</sub>	{113}<211>	75	25	45

For the purpose of modeling, yield strength values as a function of specimen orientation were normalized with respect to the yield strength value for the 0° orientation. The volume fraction of each texture component was estimated by normalizing the intensity of the component,  $f(g)_i$ , relative to the combined intensity of all of the components,  $\Sigma f(g)_i$ . Average Taylor factors were calculated as a function of tensile specimen orientation by summing the product of the Taylor factor and the volume fraction for each of the texture components examined (i.e.  $\bar{M} = M_i \cdot f(g)_i / \Sigma f(g)_i$ ). It was recognized that the Taylor factor is asymmetrical about the 0° orientation for most of the texture components examined. Since the sense of a particular component is indeterminate from ODF data, the value of Taylor factor used for both the F and R models represented the average of the variation from 0° to +90° and 0° to -90°. The average Taylor factor,  $\bar{M}$ , so computed was normalized with respect to the Taylor factor for a material displaying a random texture, namely 3.06 [20, 21, 26].

### 3. Results and Discussion

#### 3.1 Texture

In addressing the results of the texture analyses, the term intensity can be considered as the area under the orientation density curves plotted either as a function of through-thickness location for the individual components or as a function of orientation ( $\phi_2$ ) in Euler space for the texture fibers. The textural characteristics of the 2195 extrusion are summarized in Figure 7. The through-thickness variations in the intensity of the dominant DF- and RX-related texture components in the Skin regions are shown in Figures 7(a) & 7(b), respectively. The dominant DF-related components are Brass and  $S'_2$ , which exhibit uniform intensities through the  $t_0$  to  $3t/4$  region which then decrease toward the  $t_i$  location. The strongest RX-related component is Cube through the cross-section, with the Goss,  $RC_{RD1}$  and  $RC_{RD2}$  components also displaying intensity. All of the RX-related components exhibit maximum intensity at the  $t/2$  location and decrease symmetrically toward both surfaces. Similarly, the through-thickness variations in the intensity of the dominant texture components in the Base regions are shown in Figures 7(c) & 7(d). The dominant DF-related component is  $Ex_1$  with the  $Ex_2$ ,  $Ex_3$  and Cu components also displaying intensity. The intensity of the  $Ex_1$  component is at a maximum at the  $t/2$  location and gradually decreases toward the  $t_i$  and  $t_0$  locations. The variation in intensities of the  $Ex_2$ ,  $Ex_3$  and Cu components through-thickness is asymmetrical, displaying maxima at the  $t/4$  location and decreasing toward both surfaces. The RX-related components comprise a mixture of  $\{hkl\}<100>$  type components with Cube and  $RC_{RD1}$  having the highest intensity. The RX-related components do not display a systematic variation in intensity through the cross-section. The intensities of the DF-related texture fibers in the Skin and Base regions at the  $t/2$  location are compared in Figure 7(e). The Skin exhibits the  $\beta$  fiber and the Base the  $<111>$  fiber, both showing similar intensity as a function of  $\phi_2$ . The  $\beta$  fiber shows maximum intensity at the Brass orientation ( $\phi_2 = 0^\circ$  and  $45^\circ$ ) and low intensity around the Cu ( $\phi_2 = -45^\circ$ ), S ( $\phi_2 = -25^\circ$ ) and  $S'_1$  ( $\phi_2 = 20^\circ$ ) orientations. Similarly, the  $<111>$  fiber shows maximum intensity at the  $Ex_1$  orientation ( $\phi_2 = 0^\circ$  and  $45^\circ$ ) and lower intensity around the Cu ( $\phi_2 = -45^\circ$ ),  $Ex_2$  ( $\phi_2 = -25^\circ$ ) and  $Ex_3$  ( $\phi_2 = 20^\circ$ ) orientations. The intensities of the RX-related fibers in the Skin and Base regions at the  $t/2$  location are compared in Figure 7(f). The  $<100>$  fiber, common to both regions, is stronger in the Skin than in the Base. Both have maximum intensity at the Cube orientation ( $\phi = 0^\circ$ ), some intensity at the Goss orientation ( $\phi = 45^\circ$ ) and lesser intensity at the  $RC_{RD1}$  and  $RC_{RD2}$  orientations ( $\phi = 20^\circ$  and  $35^\circ$ , respectively).

Figure 8 illustrates the textural characteristics of the 2098 extrusion. Figure 8(a) shows that the dominant DF-related components in the Skin region are Brass and  $S'_2$ , with S and  $S'_1$  displaying lesser intensity. For most of the components, the through-thickness variation in intensity is not symmetrical about the mid-plane with maxima exhibited in the  $t/4$  through  $t/2$  locations and decreasing intensity toward the surfaces. The exception is the  $S'_1$  orientation, which displays a maximum at the  $3t/4$  location, but also shows decreasing intensity toward the  $t_i$  and  $t_0$  locations. Figure 8(b) reveals that the intensities of the RX-related components in the Skin are relatively weak through most of the cross-section. However, the Goss and  $RC_{RD2}$  components display significant intensity at the  $t_0$  location. The through-thickness variations in the dominant DF- and RX-related texture components in the Base region are shown in Figures 8(c) & 8(d), respectively. The dominant DF-related component is  $Ex_1$ , with the  $Ex_2$ ,  $Ex_3$  and Cu components showing moderate intensity. The intensity of the  $Ex_1$  component is highest in the  $t/4$  through  $3t/4$  region and then decreases toward both surfaces. The intensities of the  $Ex_2$ ,  $Ex_3$  and Cu components vary little for most of the cross-section, but decrease to zero at the  $t_i$  location. The dominant RX-related component is Cube, with  $RC_{RD1}$ , Goss and  $RC_{RD2}$  displaying similar but lower intensity. The through-thickness variation in Cube intensity is symmetrical about the  $t/2$  location, comprising a maximum at  $t/2$  and decreasing toward the surfaces. The intensity variation of the  $RC_{RD1}$  component is

not systematic, but exhibits a maximum at the  $3t/4$  location. The intensities of the DF- and RX-related fibers in the Skin and Base regions at  $t/2$  are compared in Figure 8(e) & 8(f), respectively. The  $\langle 111 \rangle$  fiber in the Base is slightly stronger than the  $\beta$  fiber in the Skin, with maximum intensities at the  $Ex_1$  and Brass orientations, respectively. Intensities of the other DF-related components mentioned earlier are low, corresponding to the valleys observed. The  $\langle 100 \rangle$  fiber in the Base is stronger than in the Skin, particularly at the Cube orientation. The  $\langle 100 \rangle$  fiber in the Base has maximum intensity at Cube with some intensity at the Goss orientation, whereas intensities along the length of the  $\langle 100 \rangle$  fiber in the Skin are weak.

Similarly, the textural characteristics of the 2096 extrusion are shown in Figure 9. The through-thickness variations in the dominant DF- and RX-related texture components in the Skin region are shown in Figures 9(a) & 9(b), respectively. Among the DF-related components, Brass has the highest intensity, followed by  $S'_2$ , with the  $S$  and  $S'_1$  components showing lesser intensity. The variation in intensity of Brass and  $S'_2$  is asymmetrical through the cross-section, both showing maxima in the  $t/4$  through  $t/2$  location. The intensity of all components tends to decrease to low levels at both surfaces. The Cube orientation has the highest intensity among the RX-related components, with small contributions from the other  $\{hkl\}\langle 100 \rangle$  type texture components. All of the RX-related components are weak at the surfaces and only the Cube component has significant intensity in the  $t/4$  through  $3t/4$  location. Figure 9(c) shows that the dominant DF-related component in the Base region is  $Ex_1$ , with the other  $\{hkl\}\langle 111 \rangle$  components displaying lower intensity. The intensity of the  $Ex_1$  component is highest at the  $t/2$  location and decays toward both surfaces. The remaining components have a lesser, but more uniform intensity through-thickness, exhibiting a decrease only at the  $t_1$  location. Figure 9(d) shows that amongst the RX-related components, Cube displays the highest intensity in the  $t/4$  through  $3t/4$  region, with most of the other  $\{hkl\}\langle 100 \rangle$  type components being weak. There is a contribution from the  $RC_{RDI}$  component through the cross-section, but it is negligible at the  $t/2$  location. The intensities of the DF-related fibers in the Skin and Base regions at  $t/2$  are compared in Figure 9(e). The  $\langle 111 \rangle$  fiber in the Base is marginally stronger along the length than the  $\beta$  fiber in the Skin, again with maximum intensities at the  $Ex_1$  and Brass orientations, respectively. The intensities of the RX-related fibers in the Skin and Base regions at  $t/2$  are compared in Figure 9(f). The  $\langle 100 \rangle$  fiber intensities are similar and weak for both the Skin and Base, with highest intensity at Cube and some intensity at the Goss orientation.

In summarizing the data for all three alloys, the Skin regions exhibit a  $\beta + \langle 100 \rangle$  fiber texture, dominated by the Brass and Cube components. This type of texture is frequently associated with thin section extrusions and plane strain deformation processing [10]. The Base regions exhibit a  $\langle 111 \rangle + \langle 100 \rangle$  fiber texture, dominated by the  $Ex_1$  and Cube components. This texture is often associated with thick-section extrusions and axisymmetric deformation processing [15, 16]. The relative strength of the DF- and RX-related components and fibers is important when attempting to equate the textural characteristics with mechanical behavior. Taylor analyses predict that materials with strong Brass or  $S$  textures will exhibit yield strength minima in the  $30\text{-}60^\circ$  specimen orientation range, while Cube and Goss textured materials will exhibit yield strength maxima in the same orientation range [19]. Therefore, the counteracting effect of these textural elements are expected to exert a strong influence on mechanical anisotropy. In comparing the textural characteristics in the Skin and Base regions, the area of the cross-section from  $t/4$  through  $3t/4$  will have the most impact on mechanical behavior. This corresponds to the approximate through-thickness location from which the tensile and fracture toughness specimens were extracted. Evaluating the area under the curves in Figures 7, 8 & 9, the DF-related texture of the 2195 is the simplest, with contributions from components other than Brass and  $Ex_1$  being relatively small. In the case of 2098 and 2096 the texture is more of a mixture. The  $\beta$  and  $\langle 111 \rangle$  fibers are more fully developed along the length, implying that a larger number of texture components contained within are contributing to the overall texture characteristics than in 2195. The RX-related texture is best addressed by restricting discussion to the Cube orientation, since all of the other components are relatively weak. In comparing all three alloys, the intensity of the Cube orientation within the cross-sectional area of interest is highest in the 2098 Base, but lowest in the 2098 Skin region (except for the anomalous intensity spike at the

surface). The Cube orientation possesses moderate intensity in the 2195 and 2096 in both the Skin and Base regions.

The consistent differences in textural characteristics between the Skin and Base regions for all three alloys can be attributed to the geometry-dependent variations in material flow during the extrusion process. Taylor-type models have been employed previously with some success to establish texture-processing relationships in rolled product [19, 20, 23, 26, 50, 51]. One such application of a relaxed constraint (R) model (illustrated in Figure 1) predicts the formation of the  $Ex_1$  component by allowing simultaneous shearing on the T plane in the L direction (B-type shear) and on the S plane in the L direction (C-type shear), i.e. the BC model [26]. In contrast, formation of the Brass component is predicted by allowing additional shear on the S plane in the T direction (S-type shear), i.e. the BSC model (The nomenclature employed here is that adopted in reference 26). These concepts are applicable to the material flow and resultant textures observed in the near-net-shape extrusions studied here. The L, T and S directions in rolled product are analogous to the A, C and R directions, respectively, in extruded product. During the extrusion process, the diameter of the initial donut-shaped blank is increased (and the thickness simultaneously decreased) as it passes over the mandrel within the extrusion die [32]. At the locations where the stiffeners are being formed this expansion is geometrically constrained, thereby limiting material flow in the circumferential direction. Therefore, S-type shear will be restricted culminating in the Base regions exhibiting a texture dominated by the  $Ex_1$  component and the Skin regions by the Brass component.

### 3.2 Grain Structure

The macrostructural characteristics of the 2195, 2098 and 2096 extrusions are illustrated in Figures 10, 11 & 12, respectively. The macrostructures are very similar, comprising a laminated grain structure which conforms with the geometry of the extruded cross-section. In the Skin regions, the layers of grains are parallel to the principal extrusion plane and exhibit little through-thickness variation. In the Base regions, a similar layered grain structure exists, but the contours are distorted out-of-plane toward the stiffener. In the Web of the stiffener, the layers form a ‘herring bone’ pattern and the area from  $t/2$  in the Base region up into the stiffener reflects a transition in macrostructure from that in the Skin to that characteristic of the Web region. At the  $t/2$  location in the Base, the layers form an approximately triangular array at the center of the node between the Web and the Skin. The macrostructural characteristics vary little from the mid-plane toward the inner surface of the extrusion opposite the stiffener and are similar to the majority of the Skin region. The only apparent difference between the three alloys is the apparent grain size; the 2096 being the finest, the 2195 being intermediate and the 2098 being the largest.

The microstructural and microtextural characteristics of the 2195 extrusion in the Skin and Base regions are illustrated in Figure 13. The grain morphologies typical of the  $t/2$  location are shown for the C-R and A-R planes in Figures 13(a) & (b), and the corresponding microtexture results from the A-R plane are shown in Figures 13(c) & (d). Similar data for the 2098 and 2096 extrusions are displayed in Figures 14 & 15. In all three alloys, the grains are highly elongated in the extrusion direction. Although not specifically shown in the figures, the grain aspect ratio was determined to be of the order of 100:1. In both the Skin and Base regions, the microstructures can best be described as comprising a laminated grain structure with uniform layer spacings. In the Skin regions the boundaries are well-defined, but the contoured layers in the Base regions are less distinct and the boundaries are more fragmented. There is prolific subgrain structure and some evidence of deformation and shear bands throughout the extruded cross-sections. The layers appear thinner in the Skin than in the Base regions, and the grain morphology transitions from lath-shaped in the Skin to a mixture of lath-shaped and more acicular-shaped grains in the Base.

The Skin regions are equivalent to thin-section extrusions, which typically possess highly elongated grain structures with grains exhibiting an elliptical cross-section perpendicular to the extrusion direction [10, 15, 16]. In contrast, the highly localized Base region may be likened to thick-section extrusions, due to the presence of the stiffener, which typically exhibit more fibrous microstructures consisting of highly elongated grains with circular cross-sections [10, 15, 16]. The only discernible difference in the characteristics of the three alloys is that 2098 appears to have a coarser microstructure than the other two extrusions due to the layers of grains being thicker, particularly in the Base region. In contrast to rolled product, through-thickness microstructural and textural variations were not observed to be symmetrical about  $t/2$  [36, 52-55]. As indicated, the area of interest within the extruded cross-sections for the purposes of correlation with mechanical properties was the  $t/4$  to  $3t/4$  section. In the Skin, through-thickness variations in grain structure are minimal and the microstructural characteristics documented for the  $t/2$  location are representative of 90% of the cross-section. In the Base, the presence of the stiffener causes a distortion of the layered grain structure which persists for approximately 50% of the cross-section toward  $t_s$  (stiffener side). The remainder of the cross-section possessed microstructural characteristics similar to the Skin region.

The microtexture results for each of the three alloys are consistent with the ODF data in that the Skin and Base regions both exhibit double fiber textures. In addition to revealing the textural composition on a finer scale, the microtexture data also reveal the textural distribution. The Skin regions tend to contain alternating layers of  $\langle 112 \rangle$ - and  $\langle 100 \rangle$ -oriented grains, while the Base contains alternating layers of  $\langle 111 \rangle$ - and  $\langle 100 \rangle$ -oriented grains. The texture components contained within the  $\langle 112 \rangle$  fiber are very closely related to those in the  $\beta$  fiber, in that the  $\langle 112 \rangle$  fiber contains the corresponding, idealized crystallographic orientations [37]. Combining the metallographic and microtexture data for the 2195, 2098 and 2096 extrusions, the nature of the microstructure can accurately be described as a 'lamellar' grain structure throughout the extruded cross-sections. In addition to the coarser layered grain structure in the 2098, the only other difference between the three alloys is associated with the relative intensity of the DF- and RX-related fibers. In the Skin regions, the  $\langle 112 \rangle / \langle 100 \rangle$  ratio varies from a high value of 8.3 (2096) through 2.1 (2098) to a low of 1.4 (2195). In the Base regions, the  $\langle 111 \rangle / \langle 100 \rangle$  ratio varies from a high of 1.9 (2096) through 1.8 (2195) to a very low value of 0.7 (2098). Again, these differences would be expected to have an impact on mechanical anisotropy, based on the counteracting effect of DF- and RX-related texture elements on yield strength predictions [19].

### 3.3 Tensile Properties

Typical stress-strain curves for the Skin and Base regions in the 2195, 2098 and 2096 extrusions at the  $0^\circ$ ,  $45^\circ$  and  $90^\circ$  orientations are shown in the appendix for reference; Figures A1-A6, (a-c). The tensile behavior of 2195, as a function of specimen orientation to the extrusion direction, is summarized in Figures 16(a-c). In the Skin region, ultimate and yield strengths are highest at the  $90^\circ$  orientation, slightly less at  $0^\circ$  and lower at all other orientations. The yield strength is lowest in the  $60$ - $75^\circ$  range. Correspondingly, ductility is highest at  $45^\circ$  and systematically decreases toward the  $0^\circ$  and  $90^\circ$  orientations. In the Base region, ultimate and yield strength are highest at the  $0^\circ$  orientation and lower at other orientations. The yield strength is lowest around the  $30^\circ$  orientation. Ductility is highest at  $30^\circ$  and  $60^\circ$  and lowest at the  $45^\circ$  and  $90^\circ$  orientations. The tensile properties of 2098 are summarized in Figures 17(a-c). In the Skin region, ultimate and yield strength are highest at the  $90^\circ$  orientation, slightly less in the  $0^\circ$  to  $30^\circ$  range and lowest in the  $45^\circ$ - $60^\circ$  range. Tensile ductility is highest at  $45^\circ$  and tends to decrease toward the  $0^\circ$  and  $90^\circ$  orientations, although the minimum is actually located at  $15^\circ$ . In the Base region, ultimate and yield strength are highest at the  $0^\circ$  orientation, slightly less at  $90^\circ$  and lowest at the  $30^\circ$  and  $60^\circ$  orientations. Ductility is highest at  $30^\circ$ , lowest at  $15^\circ$  and  $90^\circ$  and intermediate at other orientations. The tensile data pertaining to 2096 are shown in Figures 18(a-c). In the Skin region, ultimate and yield strength are highest at the  $90^\circ$  orientation, slightly less at  $0^\circ$  and lower at all other orientations. The ultimate strength is lowest at the  $45^\circ$  orientation, whereas the yield strength is lowest in the  $60$ - $75^\circ$  range. Fluctuations in ductility with specimen orientation are smaller and less systematic than



for 2195 and 2098. In the Skin region, ductility is highest at 45° and 75°, but lowest at the 0° orientation. In the Base region, ultimate and yield strength are highest at the 0° orientation, slightly less at 90° and lower at other orientations. Again, the yield strength is lowest in the 60-75° range and ductility is highest at 60° and low at the 30 and 90° orientations.

The orientation-dependent variations in yield strength observed are consistent with previous findings which show that the  $\langle 111 \rangle$  fiber texture equates to maximum yield strength in the longitudinal (A) direction and the  $\beta$  fiber equates to maximum yield strength in the transverse (C) direction [10, 15, 16, 56]. In the Skin regions, tensile ductility is highest for 2195, lowest for 2096 and intermediate for 2098. The orientation dependence of ductility was similar, with a consistent increase in ductility with decrease in yield strength in the off-axis orientations. In contrast, orientation-dependent fluctuations in ductility are not systematic in the Base regions. A common feature of the data is that ductility is at, or close to, a minimum at the 90° orientation for all three alloys. The data also show a drop in both yield strength and ductility in selected off-axis orientations. This anomalous tensile behavior is probably related to the influence of complex grain morphologies on fracture mode and the detrimental impact on ductility that has been documented for rolled products [57-62]. Reduced ductility in highly directional microstructures has been associated with fracture occurring by a mixture of transgranular failure along shear bands and intergranular failure along grain boundaries oriented parallel to the plane of maximum resolved shear stress [63-65]. The more fibrous nature of the grain structure in the Base region provides an increased area fraction of unfavorably oriented grain boundaries in the off-axis orientations resulting in lower ductility [66-68]. In extruded products with a similar cross-sectional geometry, it has been observed that tensile fracture tends to follow the contours of the grain structure in such regions, again reducing ductility [69-71]. The tensile properties, averaged over all orientations, are compared in Table 4, which indicates that alloy composition as a variable governs the overall strength levels only. This is to be expected based on the decreasing solute content and a common primary strengthening phase [33]. For all three alloys, the lowest strength is approximately 85% of the highest value with the maximum-minimum differential being marginally wider for the Base than for the Skin regions.

Table 4. Average Tensile and Toughness Properties

Alloy	Region	$\sigma_{UTS}$ , ksi	$\sigma_{YS}$ , ksi	el., %	$K_{J1}$ , ksi $\sqrt{\text{in}}$
2195	Skin	83	76	13	45
	Base	82	76	10	27
2098	Skin	78	71	15	41
	Base	80	71	10	30
2096	Skin	76	68	12	14
	Base	75	70	10	15

### 3.4 Fracture Toughness Properties

Typical K-R curves for the Skin and Base regions in the 2195, 2098 and 2096 extrusions at the 0°, 45° and 90° orientations are shown in the appendix for reference; Figures A1-A6, (d-f). The initiation toughness values, averaged over all orientations, are shown in Table 4. The 2195 and 2098 extrusions exhibit comparable initiation toughness, however the values for 2096 are lower. The initiation toughness values are also consistently higher for the Skin than for the Base regions in 2195 and 2098. Variations in initiation toughness with orientation for the three alloys are shown in Figures 16(d), 17(d) & 18(d), respectively. In the case of 2195, the Skin region is anisotropic exhibiting an anomalously high initiation toughness in the 45° orientation. The reason for this is unclear. The Base region is more isotropic with the lowest initiation toughness value noted in the 90° orientation. The 2098 displays similar levels of initiation toughness to 2195 in all but the 45° orientation in the Skin region. Although isotropic, the

overall level of initiation toughness in the 2096 is poor. Finally, the strength/toughness combination of these extruded products is of particular interest for structural applications. The relationship is represented in Figures 16(e), 17(e) and 18(e) for the 2195, 2098 and 2096 alloys, respectively, for both the Skin and Base regions. In general, 2195 exhibits the best combination of yield strength and initiation toughness, the 2096 extrusion the poorest, while the 2098 values are intermediate. The common feature is that there are no systematic trends in the data, regardless of alloy, location or orientation. This is in agreement with previous studies which have concluded that there is not a simple relationship between tensile ductility and fracture toughness in Al-Li alloy materials [59, 66].

In Al alloy rolled products it has been demonstrated that heavily deformed microstructures result in high L-T toughness and low T-L values, but recrystallized microstructures result in lower L-T toughness and less anisotropy [57, 58]. In Al-Li extruded plate it has also been documented that fracture toughness decreases with section thickness and increasing volume fractions of RX-related grain structure [48]. As alluded to earlier, thin-section extrusions tend to exhibit microstructures with a higher volume fraction of RX-related grains than thick-section extrusions [14, 48, 49]. The consequential changes in mechanical behavior have been cited as improved isotropy, with lower strength and toughness, but better overall ductility [72-74]. Although, it has also been shown that longitudinal ductility per se is unaffected by extruded section thickness [15, 16], the improved ductility has been equated with more equiaxed grain structures [66-68]. The 2195 and 2098 extrusions exhibit comparable levels of initiation toughness in the 0° orientation in both the Skin and Base regions, but have differing levels of RX-related textural elements. Based on the strength of the <100> fiber, the volume fraction of RX-related grains is marginally higher in the Skin than in the Base for 2195, but the reverse is true for 2098. Therefore, the trend of higher initiation toughness values in the Skin compared to the Base regions in the 2195 and 2098 extrusions, independent of orientation, is not consistent with previous observations and further study is required.

### 3.5 Texture-Yield Strength Correlations

There are many ways to correlate texture with yield strength owing to the number of descriptors available for both texture characteristics and mechanical anisotropy. In terms of texture, the intensity of dominant components, such as Brass or Cube, can be quoted, or the ratio between the two [75]. Using a broader spectrum of data, the intensity of texture fibers, such as <112>, <111> or <100>, or the ratio between them can be determined [76]. The use of ratios is often more meaningful because Taylor analysis of pure textures reveals that DF-related components, such as Brass or S, result in a yield strength minimum in the 30-60° range, while RX-related components, such as Cube and Goss, result in a maximum in the same orientation range [19]. The counteracting effect of these factors has been used to explain variations in the orientation dependence of yield strength based solely on the influence of pure texture elements. When defining anisotropy, yield strength variations have been quoted in terms of the ratio between either the minimum and maximum yield strength (i.e.  $\sigma_{ys}(\min)/\sigma_{ys}(\max)$ ), independent of specimen orientation, or simply the ratio between yield strength values at the 45° and 0° orientations (i.e.  $\sigma_{ys}(45)/\sigma_{ys}(0)$ ) [11]. In addition, a so-called ‘in-plane anisotropy’ (IPA) coefficient has been employed, which can be defined in two ways [7]. The first is for a material which is strongest parallel to the longitudinal axis (such as in the Base regions) and is defined as  $IPA = [(2 \cdot \sigma_{ys}(0) - \sigma_{ys}(45) - \sigma_{ys}(90)) / (2 \cdot \sigma_{ys}(0))] \times 100 \%$ . The second is for a material which is strongest parallel to the transverse axis (such as in the Skin regions) and is defined as  $IPA = [(2 \cdot \sigma_{ys}(90) - \sigma_{ys}(45) - \sigma_{ys}(0)) / (2 \cdot \sigma_{ys}(90))] \times 100 \%$ . Another method for quantifying anisotropy is to employ Kurtosis analysis, which is a standard mathematical tool used to describe the relative flatness of a curve [77]. In this case, it allows determination of the orientation-dependent deviations in yield strength from the average value; more negative numbers being equated with more isotropic behavior. The various descriptors for texture and yield strength used by previous authors and applied to the current data are listed in Table 5.

A survey of the data contained in Table 5 reveals that the degree of anisotropy is highly dependent on the definition employed. When using the  $\sigma_{ys}(45) / \sigma_{ys}(0)$  and  $\sigma_{ys}(\min) / \sigma_{ys}(\max)$  ratios, the 2098 Base region is the most *anisotropic* and the 2195 Base region the most *isotropic*. In contrast, when the IPA coefficient or Kurtosis analysis is employed, the 2195 Base region appears to be the most *anisotropic* and the 2096 Skin region the most *isotropic*. The rankings derived by using the various approaches are shown in Table 6, categorized into Skin and Base regions for correlation purposes. Based on the assumption that increasing amounts of RX-related texture elements should result in more isotropic yield strength behavior [19], there should be a correlation between the rankings listed in Table 6.

Table 5. Texture Characteristics @ t/2 vs. Yield Strength Anisotropy

SKIN				
Alloy		2195	2098	2096
Texture (Components)	Cube, f(g)	17	4	9
	Brass, f(g)	31	26	30
	Cube / Brass	0.55	0.15	0.30
Micro-texture (Fibers)	<100>, %	34	26	10
	<112>, %	46	54	82
	<100> / <112>	0.74	0.48	0.12
Yield Strength	$\sigma_{ys}(45) / \sigma_{ys}(0)$	0.87	0.85	0.85
	$\sigma_{ys}(\min) / \sigma_{ys}(\max)$	0.82	0.83	0.83
	IPA, %	9.8	9.9	8.6
	Kurtosis	-0.54	-0.93	-1.11
BASE				
Alloy		2195	2098	2096
Texture (Components)	Cube, f(g)	10	31	11
	$Ex_1$ , f(g)	31	34	33
	Cube / $Ex_1$	0.32	0.91	0.33
Micro-texture (Fibers)	<100>, %	28	57	29
	<111>, %	51	38	55
	<100> / <111>	0.55	1.50	0.53
Yield Strength	$\sigma_{ys}(45) / \sigma_{ys}(0)$	0.81	0.88	0.83
	$\sigma_{ys}(\min) / \sigma_{ys}(\max)$	0.79	0.83	0.80
	IPA, %	17.8	9.3	10.6
	Kurtosis	+3.26	-0.15	-0.85

Examination of the results for the Skin region reveals that increasing Cube/Brass ratio and/or <100>/<112> ratio correlates with increasing yield strength isotropy as defined by the  $\sigma_{ys}(\min)/\sigma_{ys}(\max)$  ratio. Inversely, increasing Cube/Brass ratio and/or <100>/<112> ratio correlates with decreasing yield strength isotropy as defined by the  $\sigma_{ys}(45)/\sigma_{ys}(0)$  ratio. In the case of the Base region, the rankings show that increasing Cube/  $Ex_1$  ratio correlates with increasing yield strength isotropy as defined by the IPA coefficient. However, increasing Cube/  $Ex_1$  ratio correlates with decreasing yield strength isotropy as defined by both the  $\sigma_{ys}(45)/\sigma_{ys}(0)$  and  $\sigma_{ys}(\min)/\sigma_{ys}(\max)$  ratios. The net result from these observations is that there is no systematic trend based on the commonly used descriptors and an alternative approach is required.

The results of applying the F (Taylor) and IGD (Wert) models to single grains with orientations commonly observed in the present work are shown in Figure 19. The texture components selected were Brass, {011}<211>;  $Ex_1$ , {011}<111>; and Cube, {001}<100>; and predicted values of Taylor factor are

Table 6. Texture/Anisotropy Rankings

SKIN	Cube/ Brass	$\langle 100 \rangle /$ $\langle 112 \rangle$	$\sigma_{ys}(45) /$ $\sigma_{ys}(0)$	$\sigma_{ys}(\min) / \sigma_{ys}(\max)$	IPA, %	Kurtosis	
Least RX	2098	2096	2195	2098	2098	2195	Least Iso.
	2096	2098	2098	2096	2195	2098	
Most RX	2195	2195	2096	2195	2096	2096	Most Iso.
BASE	Cube/ Ex <sub>1</sub>	$\langle 100 \rangle /$ $\langle 111 \rangle$	$\sigma_{ys}(45) /$ $\sigma_{ys}(0)$	$\sigma_{ys}(\min) / \sigma_{ys}(\max)$	IPA, %	Kurtosis	
Least RX	2195	2096	2098	2098	2195	2195	Least Iso.
	2096	2195	2096	2096	2096	2098	
Most RX	2098	2098	2195	2195	2098	2096	Most Iso.

compared as a function of tensile axis orientation. The plots reveal that at certain specimen orientations, there are large differences in the Taylor factor values predicted by the two models. The Brass-oriented grain shows the largest difference around the  $-55^\circ$  orientation, Ex<sub>1</sub> around the  $-35^\circ$  orientation and Cube around the  $\pm 45^\circ$  orientations. The three grain types have one thing in common at these orientations, in that a  $\langle 110 \rangle$  direction in each of these grains is oriented parallel to the tensile axis. The significance of this is that the tendency for an individual grain to depart from axisymmetric flow is dependent on orientation with respect to the tensile axis [75]. The ratio between the Taylor factor and the reciprocal of the Schmid factor is unity (i.e.  $M/(1/m) = 1$ ) for grains with  $\langle 100 \rangle$  or  $\langle 111 \rangle$  parallel to the tensile axis. However,  $M/(1/m) > 1$  at other grain orientations and is close to the maximum ( $M/(1/m) = 1.65$ ) when  $\langle 110 \rangle$  is parallel to the tensile axis [20]. So it is expected  $\langle 110 \rangle$ -oriented grains have much lower predicted values of yield strength and the largest tendency to deviate from the F model toward the N model and would be better predicted by an R-type (or the IGD) model.

Average Taylor factors calculated for all three extrusions in both the Skin and Base regions employing the F and IGD models are shown in Figure 20. As described earlier, Taylor factors as a function of orientation for bulk material were determined using a weighted average including all of the texture components considered. The asymmetry with respect to orientation, which is common to most of the components, was accounted for by averaging the variation from  $0^\circ$  to  $+90^\circ$  with that from  $0^\circ$  to  $-90^\circ$ . The dotted line on the plots represents the Taylor factor for a fully isotropic material comprising a randomly oriented grain structure, i.e.  $\bar{M} = 3.06$  [20, 21, 26]. The Skin and Base regions show many common trends for all three alloys. The F model predictions for the average Taylor factor are consistently higher than the IGD model, independent of specimen orientation. The F model also predicts that approximately half of the orientations will have a higher Taylor factor than a specimen with a random grain structure. With a few exceptions, the IGD model predicts that the average Taylor factor will be lower than that for a random sample at all orientations. Both models predict that the Taylor factor will be at a maximum at the  $90^\circ$  orientation in the Skin and at the  $0^\circ$  orientation in the Base for all of the extrusions. Both models also predict a single minimum, but the location with respect to specimen orientation varies. According to the F model, the specimen orientation at which the minimum Taylor factor is predicted varies widely. However, the IGD model predicts a minimum in the  $45$ - $60^\circ$  orientation range in the Skin and the  $30$ - $45^\circ$  range in the Base. This can be explained by revisiting Figures 19(a) and 19(b), which show the variation for the dominant texture components in the Skin (Bs) and Base (Ex<sub>1</sub>) regions, respectively. The largest difference between the F and IGD model predictions is in the  $-45$  to  $-60^\circ$  specimen orientation range for Bs and the  $-30$  to  $-45^\circ$  range for the Ex<sub>1</sub> component. Averaging the Taylor factor values between  $-90^\circ$  and  $+90^\circ$  to arrive at  $\bar{M}$  for the bulk results in a single and very pronounced minimum in the  $45$ - $60^\circ$  range in the Skin and the  $30$ - $45^\circ$  range in the Base.

The yield strength as a function of specimen orientation, normalized with respect to the yield strength value for the  $0^\circ$  orientation, is also shown in Figure 20. A comparison between the measured and predicted values of yield strength reveals that application of the model concepts explored by Wert and co-workers show promise [30, 31]. The overall validity of the model can be judged by its ability to predict, (a), the orientations at which highs and lows in yield strength occur, and (b), the absolute magnitude of the highs and lows. For all three extrusions, in both the Skin and Base regions, the IGD model predictions agree well with both the location and the magnitude of the fluctuations in measured yield strength. The IGD model provides a much better simulation than the F model, which is consistent with previous studies employing progressively relaxed constraints with increasing grain aspect ratio in order to accurately predict yield strength anisotropy [19, 20, 23, 26, 50, 51]. Such models assume that five active slip systems are required to support deformation of equiaxed grain structures and that, as the grain aspect ratio increases, the number of necessary slip systems decreases. On this basis, the F model is only expected to be accurate for materials with equiaxed grain structures and the IGD model will tend to work better for flat and/or elongated grain structures. The highly directional, lamellar grain structure characteristic of all three extrusions easily falls into this latter microstructural category.

It is probable that no single model can accurately simulate yield strength anisotropy in materials containing highly elongated grain structures. Model predictions for such materials tend to be artificial because it has to be assumed that the grain direction is always parallel to the tensile axis [23, 50]. In reality, when the tensile axis is parallel to the grain direction ( $0^\circ$ ), the grains are being loaded in *parallel* and the situation is close to homogeneous strain in all grains. In contrast, when the tensile axis is perpendicular to the grain direction ( $90^\circ$ ), the grains are being loaded in *series* and the situation is close to uniform stress in all grains [20]. Consequently, the F model is applicable at  $0^\circ$ , the N model is more appropriate at  $90^\circ$  and a composite of the two should provide the best predictions at intermediate specimen orientations, i.e. an R-type model. In this case, that was only found to be true for the 2098 Skin region, where Figure 20(c) shows that the F model provides a better simulation for the  $0$ - $30^\circ$  orientations and the IGD model is more accurate for higher specimen orientations. Both of these models assume that the microstructure is homogeneous and that there is no interaction between grains. However, the microstructure in both the Skin and Base regions essentially comprises a laminate of alternating layers of DF- and RX- related grains. The interaction between grains in these multi-layered microstructures may account for the discrepancies between predicted and measured yield strength anisotropy observed.

Grain morphology as a variable, contributing to relaxed constraints, was not specifically accounted for in this application of the IGD model. Despite the omission, the data clearly demonstrate that the IGD model provides a better simulation of yield strength anisotropy in the three extrusions than the F model. This suggests that the key assumption of the model, namely minimum yield strength in each grain, is appropriate for predicting the behavior of materials exhibiting lamellar grain structures. Predictions by the IGD model also tended to be more accurate for the Skin regions than for the Base regions, and this is probably related to the highly localized nature of the area beneath the stiffeners. The Skin region exhibited much more uniform microstructural and textural characteristics than the Base region. As indicated earlier, the Base texture sample was constructed as a laminate in order to isolate the texture characteristics at that location. Such compensation could not be made with the tensile specimens with gage dimensions larger than the extent of the Base region. At the  $0^\circ$  orientation, the Base region constitutes 100% of the gage length and 50% of the gage width, but at the  $90^\circ$  orientation, only 12.5% of the gage length and 100% of the gage width (Figure 6). Therefore, the yield strength data pertaining to the Base region is likely compromised by contributions from, and interactions with, neighboring Skin regions which currently cannot be incorporated into models [52, 53].

## 4. Concluding Remarks

An investigation of the structure-property relationship in Al-Li alloy extrusions has been conducted. The microstructural characteristics of the 2195, 2098 and 2096 extrusions are similar, comprising a *laminar* structure of high aspect ratio grains exhibiting location-dependent variations in morphology. 2098 had the coarsest grain structure and 2096 the finest throughout the extruded cross-sections. The differences in grain structure between the Skin and Base regions can be attributed to variations in material flow during the extrusion process. The Skin region is equivalent to a thin section extrusion, resulting in lath-shaped grains arranged in parallel layers. The highly localized Base region is effectively a thick section extrusion, due to the presence of the stiffeners, resulting in a mixture of lath-shaped and acicular-shaped grains. The textural composition of the three extrusions is also similar, all exhibiting a double fiber texture throughout. The Skin regions exhibit a  $\beta + \langle 100 \rangle$  fiber texture, concentrated at the Brass and Cube orientations, which is frequently associated with plane strain deformation processing. The Base regions exhibit a  $\langle 111 \rangle + \langle 100 \rangle$  fiber texture, concentrated at the Ex<sub>1</sub> and Cube orientations, which is often associated with axisymmetric deformation processing. The textural distribution, revealed by the microtexture results, comprises alternating layers of  $\langle 112 \rangle$ - and  $\langle 100 \rangle$ -oriented grains in the Skin regions and alternating layers of  $\langle 111 \rangle$ - and  $\langle 100 \rangle$ -oriented grains in the Base regions. In combination with the metallographic observations, the microstructure can be accurately described as a *lamellar* grain structure.

The tensile behavior of the 2195, 2098 and 2096 extrusions share several common characteristics. The Skin regions are strongest in the 90° orientation and weakest in the 50°-75° specimen orientation range. In contrast, the Base regions are strongest in the 0° orientation and weakest near the 30° and 60° specimen orientations. Independent of specimen orientation, the minimum yield strength is approximately 85% of the maximum value in all three extrusions, being consistently higher in the Base regions than the Skin regions. In both the Skin and Base regions, 2195 exhibits the highest strength, but is the most anisotropic, 2098 has lower strength, but is more isotropic, and 2096 has the lowest strength, but is the most isotropic. The fracture toughness data reveal that 2195 and 2098 exhibit comparable initiation toughness, while the values for 2096 are poor. The Skin regions exhibit highest toughness in the 45°(45-45) orientations and lowest in the 90°(C-A) orientations. The Base regions exhibit the best toughness in the 0°(A-C) orientations and the lowest in the 90° orientations. Fracture toughness properties are consistently better in the Skin regions than in the Base regions, which is probably related to the complex grain structure observed in the Base. The more acicular grain morphology presents a higher area fraction of unfavorably oriented grain boundaries for 45° and 90° specimen orientations.

Attempts to correlate yield strength anisotropy with textural characteristics based on commonly used descriptors were not successful. The degree of anisotropy proved to be highly dependent on the definition employed and ranking of the alloys revealed no consistent trends. In contrast to previous findings, there was also no apparent correlation between increasing amounts of RX-related texture elements and more isotropic yield strength behavior. Application of the modeling concepts explored by Wert et al. showed some promising results. The relaxed constraint (IGD) model consistently provided better simulations of the yield strength anisotropy than the full constraint (F) model for all three extrusions. This implies that relaxing the axisymmetric strain requirement, reducing the number of necessary slip systems and assuming minimum yield strength in each grain is appropriate for materials comprising lamellar microstructures. The Wert model predictions for the Skin region tended to be more accurate than for the Base regions because the grain morphology and textural composition were more uniform. Deviations between the predicted and measured anisotropy were likely a consequence of the heterogeneous microstructures observed and the effects of gradient microstructures will need to be incorporated into future models.

## 5. Acknowledgements

The authors would like to acknowledge various contributions to this work; raw texture data, courtesy of J.A. Alexa; optical metallography, courtesy of J.M. Baughman; microtexture data, courtesy of R.E. Crooks; critical review of the manuscript, courtesy of R.N. Shenoy; all with Analytical Services and Materials, Inc., Hampton, Virginia.

## 6. References

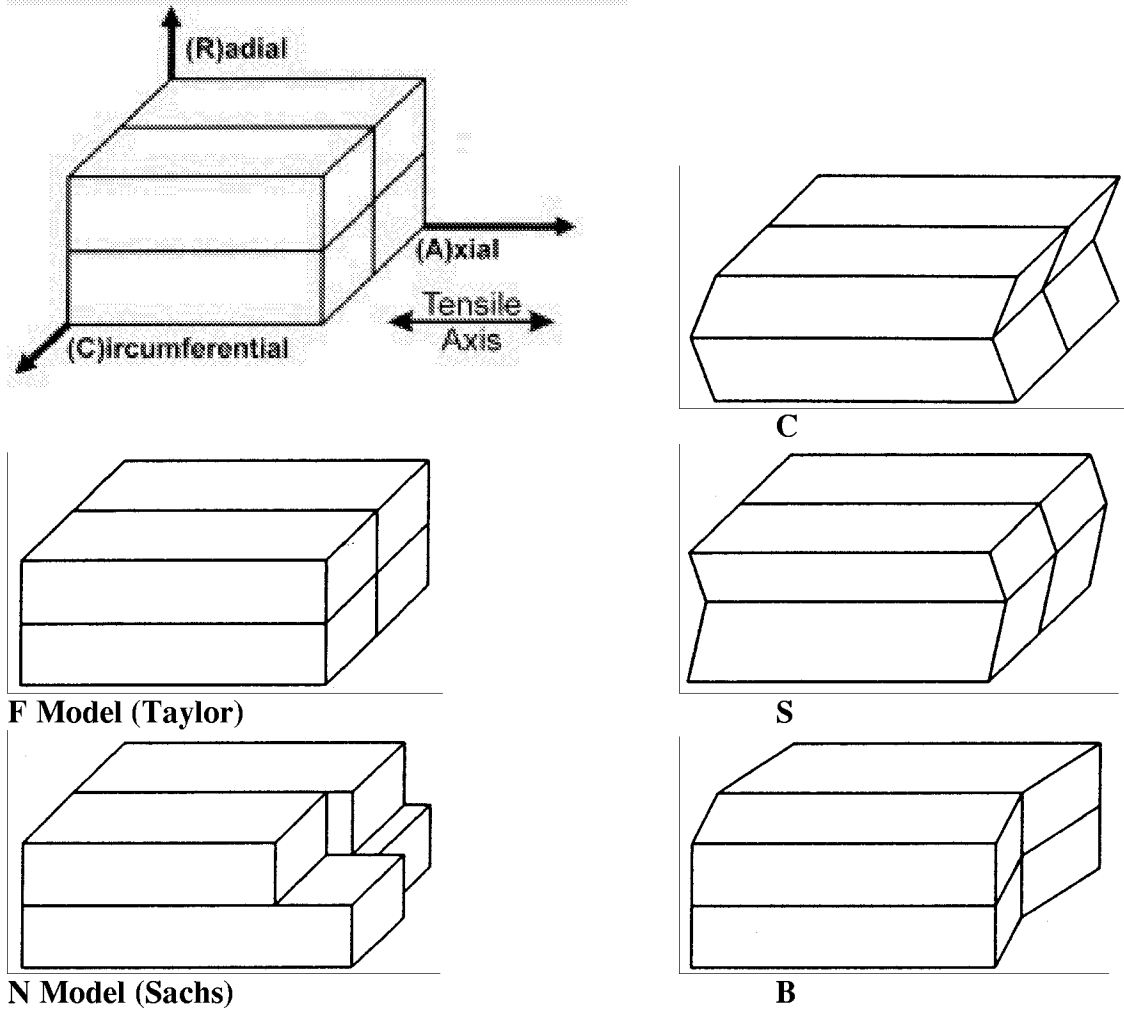
1. M.J. Birt, M.S. Domack, R.A. Hafley and W.D. Pollock, *Characterization of Al-Cu-Li Alloy 2090 Near Net Shape Extrusion*, NASA Technical Memorandum, TM-1998-207668, Hampton, VA, May 1998.
2. S.J. Hales and R.A. Hafley, "Texture and anisotropy in Al-Li alloy 2195 plate and near-net-shape extrusions", *J. Mater.Sci.& Engng. A*, vol.257, no.1, 1998, pp. 153-164.
3. R.S. James, "Aluminum-lithium alloys", in *Metals Handbook, Tenth Edition*, ASM International, Metals Park, OH, vol.2, 1990, pp. 178-199.
4. W.E. Quist and G.H. Narayanan, "Aluminum-lithium alloys", in *Aluminum Alloys - Contemporary Research and Applications*, A.K. Vasudevan and R.D. Doherty (eds.), Treatise on Materials Science and Technology, Academic Press, San Diego, CA, vol.31, 1989, pp. 219-254.
5. O. Engler, J. Mizera, J. Driver and K. Lücke, "Texture and plastic anisotropy in Al-Li model alloys", in *Aluminium-Lithium VI*, M. Peters and P.-J. Winkler (eds.), DGM, Oberursel, Germany, 1992, pp. 307-314.
6. F.W. Gayle, W.T. Tack, G. Swanson, H.F. Heubaum and J.R. Pickens, "Composition and Anisotropy in Al-Cu-Li-Ag-Mg-Zr Alloy", *Scripta Metall. et Mater.*, vol.30, no.6, 1994, pp. 761-766.
7. K.V. Jata, A.K. Hopkins and R.J. Rioja, "The anisotropy and texture of Al-Li alloys", in *Proceedings of the 5th International Conference on Aluminium Alloys (ICAA5)*, J.H. Driver et al. (eds.), Trans Tech Publications Ltd., Switzerland, 1996, pp. 647-652.
8. A.K. Vasudevan, W.G. Fricke, M.A. Przystupa and S. Panchanadeeswaran, "Synergistic effects of crystallographic texture and precipitation on the yield stress anisotropy in Al-Li-Cu-Zr alloy", in *Proceedings of the 8th International Conference on Textures of Materials (ICOTOM 8)*, J.S. Kallend and G. Gottstein (eds.), TMS, Warrendale, PA, 1988, pp. 1071-1077.
9. W. Calles and G. Tempus, "Extrusion, Heat Treatment and Mechanical Properties of Al-Li Alloys", *J. Materialien*, vol.1, 1993, pp. 9-13.
10. D.K. Denzer, P.A. Hollinshead, J. Liu, K.P. Armanie and R.J. Rioja, "Texture and properties of 2090, 8090 and 7050 extruded products", in *Aluminium-Lithium VI*, M. Peters and P.-J. Winkler (eds.), DGM, Oberursel, Germany, 1992, pp. 903-908.
11. K.V. Jata, S. Panchanadeeswaran and A.K. Vasudevan, "Evolution of texture, microstructure and mechanical property anisotropy in an Al-Li-Cu alloy", *J. Mater.Sci.& Engng. A*, vol.257, no.1, 1998, pp. 37-46.
12. R.J. Rioja, "Fabrication methods to manufacture isotropic Al-Li alloys and products for space and aerospace applications", *J. Mater.Sci.& Engng. A*, vol.257, no.1, 1998, pp. 100-107.
13. A.K. Mukhopadhyay, H.M. Flower and T. Sheppard, "Variation in structure and properties in an Al-Li-Cu-Mg-Zr alloy produced by extrusion processing", in *Aluminum-Lithium IV*, J. de Physique, Colloque C3, Supplement au n°9, Tome 48, Septembre 1987, pp. 219-228.
14. M.J. Tan and T. Sheppard, "Extrusion processing of an Al-Li-Cu-Mg alloy AA2091", in *Aluminum-Lithium IV*, J. de Physique, Colloque C3, Supplement au n°9, Tome 48, Septembre 1987, pp. 209-218.
15. G. Tempus, W. Calles and G. Scharf, "Influence of extrusion process parameters and texture on mechanical properties of Al-Li extrusions", *J. Mater.Sci.& Tech.*, vol.7, no.10, 1991, pp. 937-945.
16. G. Tempus, G. Scharf and W. Calles, "Influence of extrusion process parameters on the mechanical properties of Al-Li extrusions", in *Aluminum-Lithium IV*, J. de Physique, Colloque C3, Supplement au n°9, Tome 48, Septembre 1987, pp. 187-193.
17. R. Crooks, Z. Wang, V.I. Levit and R.N. Shenoy, "Microtexture, microstructure and plastic anisotropy of AA2195", *J. Mater.Sci.& Engng. A*, vol.257, no.1, 1998, pp. 145-152.
18. J. Mizera, J.H. Driver, E. Jezierska and K. Kurzydowski, "Studies of the relationship between the microstructure and anisotropy of the plastic properties of industrial aluminum-lithium alloys", *J. Mater.Sci.& Engng. A*, vol.212, no.1, 1996, pp. 94-101.

19. W.G. Fricke and M.A. Przystupa, "Texture", in *Aluminum Alloys - Contemporary Research and Applications*, A.K. Vasudevan and R.D. Doherty (eds.), Treatise on Materials Science and Technology, Academic Press, San Diego, CA, vol.31, 1989, pp. 563-578.
20. W.F. Hosford, *The Mechanics of Crystals and Textured Polycrystals*, Oxford University Press, New York, NY, 1993.
21. G.I. Taylor, "Plastic strain in metals", *J. Inst. Metals*, vol.62, 1938, pp. 307-324.
22. J.F.W. Bishop, "A theory of the tensile and compressive textures of face-centred cubic metals", *J. Mech. & Phys. Solids*, vol.3, 1954, pp. 130-142.
23. M.A. Przystupa, A.K. Vasudevan and W.G. Fricke, "Application of the relaxed constraints model to the prediction of plastic anisotropy", in *Proceedings of the 8th International Conference on Textures of Materials (ICOTOM 8)*, J.S. Kallend and G. Gottstein (eds.), TMS, Warrendale, PA, 1988, pp. 1051-1057.
24. H.-J. Bunge, *Texture Analysis in Materials Science*, Butterworths, London, 1982.
25. G.J. Davies, D.J. Goodwill and J.S. Kallend, "Charts for analysing crystallite distribution function plots for cubic materials", *J. Appl. Cryst.*, vol.4, 1971, pp. 67-70.
26. J. Hirsch and K. Lücke, "Mechanism of deformation and development of rolling textures in polycrystalline f.c.c. metals", Parts I and II, *Acta Metall.*, vol.36, no.11, 1988, pp. 2863-2882 and 2883-2904.
27. M.T. Lytle, *Precipitate-Induced Yield Anisotropy*, Ph.D. Thesis, University of Virginia, Charlottesville, VA, May 1997.
28. M.T. Lytle and J.A. Wert, "The plastic anisotropy of an Al-Li-Cu-Zr alloy extrusion in unidirectional deformation", *Metall. & Mater. Trans. A*, vol.27A, no.11, 1996, pp. 3503-3512.
29. M.T. Lytle and J.A. Wert, "Precipitate-induced plastic anisotropy: explicit solutions of the plastic anisotropy due to plate-shaped precipitates", *Metall. & Mater. Trans. A*, vol.30A, no.5, 1999, pp. 1283-1288.
30. T.S. Anderegg, *Localized Yield Strength and Fracture Toughness in an Integrally Stiffened Aluminum Alloy Extrusion*, M.S. Thesis, University of Virginia, Charlottesville, VA, January 2000.
31. T.S. Anderegg and J.A. Wert, "Effect of strain state on a yield anisotropy model for materials strengthened by plate-shaped precipitates", in *Proceedings of the 7th International Conference on Aluminum Alloys (ICAA7)*, E.A. Starke, T.H. Sanders and W.A. Cassada (eds.), Trans Tech Publications, Switzerland, 2000, pp. 1267-1272.
32. P.J. Hartley, *Production of Aluminum-Lithium Near Net Shape Extruded Cylinders*, NASA Contractor Report 198204, Lockheed Martin Manned Space Systems, New Orleans, LA, September 1995.
33. A. Cho, R.E. Greene, M.H. Skillingberg and P.S. Fielding, "Al-Li alloy development at Reynolds Metals Company for aerospace applications", in *Aluminum-Lithium Alloys for Aerospace Applications Workshop*, B.N. Bhat, T.T. Bales and E.J. Vesely (eds.), NASA Conference Publication 3287, Marshall Space Flight Center, AL, December 1994, pp. 17-25.
34. F. Barlat, J.C. Brem and J. Liu, "On crystallographic texture gradient and its mechanical consequences in rolled aluminum-lithium sheet", *Scripta Metall. et Mater.*, vol.27, no.9, 1992, pp. 1121-1126.
35. F. Barlat, S.M. Miyasato, J. Liu and J.C. Brem, "On crystallographic texture and anisotropy in Al-Li sheet", in *Proceedings of the 4th International Conference on Aluminum Alloys (ICAA4)*, T.H. Sanders and E.A. Starke (eds.), Georgia Institute of Technology, Atlanta, GA, 1994, Vol. II, pp. 389-396.
36. R. Doglione, S. Spriano and D. Firrao, "Mechanical characteristics of AA 8090-T8 with microstructural gradients", in *Proceedings of the 5th International Conference on Aluminium Alloys (ICAA5)*, J.H. Driver et al. (eds.), Trans Tech Publications Ltd., Switzerland, 1996, pp. 1061-1066.
37. L. Viviani, G. Caglioti, G. Albertini, M. Ceretti, F. Fiori and F. Rustichelli, "Texture and mechanical anisotropy of 6082 Al alloy samples subjected to extrusion and rolling", in *Proceedings of the 5th International Conference on Aluminium Alloys (ICAA5)*, J.H. Driver et al. (eds.), Trans Tech Publications Ltd., Switzerland, 1996, pp. 653-658.
38. I.L. Dillamore and W.T. Roberts, "Crystallographic texture variation through rolled aluminium and copper sheet", *J. Inst. Met.*, vol. 92, 1963-64, pp. 193-199.
39. O. Engler and K. Lücke, "Mechanisms of recrystallization texture formation in aluminum alloys", *Scripta Metall. et Mater.*, vol.27, no.11, 1992, pp. 1527-1532.
40. O. Engler, D. Ponge, W. Schelb, K. Welpmann, M. Peters and K. Lücke, "Investigations on texture in damage tolerant 8090 Al-Li sheet", in *Aluminium-Lithium VI*, M. Peters and P.-J. Winkler (eds.), DGM, Oberursel, Germany, 1992, pp. 333-338.
41. K. Lücke and O. Engler, "Effects of particles on development of microstructure and texture during rolling and recrystallization in f.c.c. alloys", *J. Mater. Sci. & Tech.*, vol.6, no.11, 1990, pp. 1113-1130.
42. B. Ren and J.G. Morris, "Microstructure and texture evolution of Al during hot and cold rolling", *Metall. & Mater. Trans. A*, vol.26A, no.1, 1995, pp. 31-40.
43. ASTM E8-96, "Standard Test Methods for Tension Testing of Metallic Materials", *Annual Book of ASTM Standards*, West Conshohocken, PA, Vol. 03.01, 1996, pp. 55-75.



44. ASTM E813-89, "Standard Test Method for  $J_{IC}$ , A Measure of Fracture Toughness", *Annual Book of ASTM Standards*, West Conshohocken, PA, Vol. 03.01, 1996, pp. 633-647.
45. ASTM E1152-95, "Standard Test Method for Determining J-R Curves", *Annual Book of ASTM Standards*, West Conshohocken, PA, Vol. 03.01, 1996, pp. 750-760.
46. J.B. Barsom and S.T. Rolfe, *Fracture and Fatigue Control in Structures*, Prentice-Hall, Inc., Englewood Cliffs, NJ, 1987.
47. P.C. Paris, H. Tada, A. Zahoor and H. Ernst, "The theory of instability of the tearing mode of elastic-plastic crack growth", in *Elastic-Plastic Fracture, ASTM STP 668*, J.D. Landes, J.A. Begley and G.A. Clarke (eds.), American Society for Testing and Materials, West Conshohocken, PA, 1979, pp. 5-36.
48. M.A. Reynolds and E. Creed, "The development of 8090 and 8091 alloy extrusions", in *Aluminum-Lithium IV*, J. de Physique, Colloque C3, Supplement au n°9, Tome 48, Septembre 1987, pp. 195-207.
49. M.H. Skillingberg and R.F. Ashton, "Processing and performance of Al-Li-Cu-X extrusions", in *Aluminum-Lithium IV*, J. de Physique, Colloque C3, Supplement au n°9, Tome 48, Septembre 1987, pp. 179-186.
50. M.A. Przystupa, A.K. Vasudevan and A.D. Rollett, "Crystallographic texture gradients in the aluminum 8090 matrix alloy and 8090 particulate composites", *J. Mater.Sci.& Engng.*, vol.A186, 1994, pp. 35-44.
51. A.K. Vasudevan, M.A. Przystupa and W.G. Fricke, "Effect of composition on crystallographic texture in hot-rolled Al-Li-Cu alloys", *J. Mater.Sci.& Engng.*, vol.A208, 1996, pp. 172-180.
52. V. Ocenasek, K. Sperlink, P. Zuna and K. Macek, "Heterogeneity and anisotropy of mechanical and fatigue properties of high-strength aluminium extrusions", in *Proceedings of the 6th International Conference on Aluminum Alloys (ICAA6)*, T. Sato, S. Kumai, T. Kobayashi and Y. Murakami (eds.), Japan Institute of Light Metals, Tokyo, Japan, 1998, pp. 1313-1318.
53. I.N. Fridlyander, V.F. Shamrai, A.A. Babareko and O.A. Setiukov, "The texture and mechanical properties of Al-Li alloy semi-products", in *Proceedings of the 6th International Conference on Aluminum Alloys (ICAA6)*, T. Sato, S. Kumai, T. Kobayashi and Y. Murakami (eds.), Japan Institute of Light Metals, Tokyo, Japan, 1998, pp. 1299-1304.
54. S. Spriano, R. Doglione, M. Baricco, L. Battezzati and D. Firrao, "Microstructural and thermal analysis of AA 8090 plate alloy with crystallographic texture gradient", in *Proceedings of the 5th International Conference on Aluminium Alloys (ICAA5)*, J.H. Driver et al. (eds.), Trans Tech Publications Ltd., Switzerland, 1996, pp. 1067-1072.
55. A.K. Vasudevan, W.G. Fricke, R.C. Malcolm, R.J. Bucci, M.A. Przystupa and F. Barlat, "On through thickness texture gradient in Al-Li-Cu-Zr alloy", *Metall. Trans. A*, vol. 19A, no. 3, 1988, pp. 731-732.
56. S.J. Harris, B. Noble and A. Dodd, "The effect of texture on the tensile and fatigue properties of 8090 plate alloys", in *Aluminum-Lithium V*, T.H. Sanders and E.A. Starke (eds.), MCEP Ltd., Birmingham, UK, 1989, pp. 1061-1075.
57. A.W. Bowen, K.M. Gatenby, D.S. McDarmaid and I.G. Palmer, "Influence of recrystallized grain structure and texture on the mechanical properties of damage tolerant 8090 Al-Li alloy sheet", in *Aluminium-Lithium VI*, M. Peters and P.-J. Winkler (eds.), DGM, Oberursel, Germany, 1992, pp. 327-332.
58. I.G. Palmer, W.S. Miller, D.J. Lloyd and M.J. Bull, "Effect of grain structure and texture on mechanical properties of Al-Li base alloys", in *Aluminium-Lithium Alloys III*, C. Baker, P.J. Gregson, S.J. Harris and C.J. Peel (eds.), The Institute of Metals, London, UK, 1986, pp. 565-575.
59. E.J. Lavernia, T.S. Srivatsan and F.A. Mohamed, "Strength, deformation, fracture behavior and ductility of aluminium-lithium alloys", *J. Mater.Sci.*, vol.25, 1990, pp. 1137-1158.
60. W.S. Miller, M.P. Thomas, D.J. Lloyd and D. Creber, "Deformation and fracture in Al-Li base alloys", in *Aluminium-Lithium Alloys III*, C. Baker, P.J. Gregson, S.J. Harris and C.J. Peel (eds.), The Institute of Metals, London, UK, 1986, pp. 584-594.
61. A.K. Vasudevan and R.D. Doherty, "Grain boundary ductile fracture in precipitation hardened aluminum alloys", *Acta Metall.*, vol.35, no.6, 1987, pp. 1193-1219.
62. A.K. Vasudevan, R.D. Doherty and S. Suresh, "Fracture and fatigue characteristics in aluminum alloys", in *Aluminum Alloys - Contemporary Research and Applications*, A.K. Vasudevan and R.D. Doherty (eds.), Treatise on Materials Science and Technology, Academic Press, San Diego, CA, vol.31, 1989, pp. 445-462.
63. A. Kumar, R.K. Prasad and E.S. Dwarakadasa, "Anisotropic tensile and fracture behaviour of aluminium lithium alloy 8090", *J. Met.& Mater.Proc.*, vol.2, no.4, 1991, pp. 279-292.
64. N.E. Prasad, S.V. Kamat, G. Malakondaiah and V.V. Kutumbarao, "In-plane anisotropy in the fracture toughness of an Al-Li 8090 alloy plate", *J. Engng.Frac.Mech.*, vol.46, no.2, 1993, pp. 209-223.
65. N.E. Prasad and G. Malakondaiah, "Anisotropy of mechanical properties in quaternary Al-Li-Cu-Mg alloys", *Bull.Mater.Sci.(India)*, vol.15, no.4, 1992, pp. 297-310.

66. R.C. Dorward, "Fracture behavior of commercial Al-Li alloys", in *Advances in Fracture Research*, K. Salama, K. Ravi-Chandar, D.M.R. Taplin and P. Rama Rao (eds.), Pergamon Press, NY, 1989, pp. 2413-2422.
67. N.E. Prasad, K.S. Prasad, S.V. Kamat and G. Malakondaiah, "Influence of microstructural features on the fracture resistance of aluminium-lithium alloy sheets", *J. Engng.Fract.Mech.*, vol.51, no.1, 1995, pp. 87-96.
68. T.S. Srivatsan, T.A. Place and T.S. Sudarshan, "Microstructural effects governing the fracture behavior of Al-Li-Cu-Mg alloy 8090", in *Advances in Fracture Research*, K. Salama, K. Ravi-Chandar, D.M.R. Taplin and P. Rama Rao (eds.), Pergamon Press, NY, 1989, pp. 2611-2621.
69. F. Broussaud and C. Diot, "Influence of grain morphology and texture on the deformation and fracture of extruded CP276 Al-Li alloy", in *Aluminum-Lithium IV*, J. de Physique, Colloque C3, Supplement au n°9, Tome 48, Septembre 1987, pp. 597-603.
70. W.D. Pollock and S.J. Hales, "Tensile fracture of a 2090 extrusion", in *Proceedings of the 4th International Conference on Aluminum Alloys (ICAA4)*, T.H. Sanders and E.A. Starke (eds.), Georgia Institute of Technology, Atlanta, GA, 1994, Vol. II, pp. 358-365.
71. A.J. Trowsdale, B. Noble, S.J. Harris, J. White and I.G. Palmer, "Effect of microstructure on tensile and fracture properties of aluminium alloys with high lithium content", *J. Mater.Sci.& Tech.*, vol.11, no.3, 1995, pp. 237-244.
72. V. Ocenasek, K. Sperlink, I.N. Frydlyander and L.N. Leshiner, "Inhomogeneity of mechanical and fatigue properties of Al-Li alloy extrusions", in *Proceedings of the 5th International Conference on Aluminium Alloys (ICAA5)*, J.H. Driver et al. (eds.), Trans Tech Publications Ltd., Switzerland, 1996, pp. 1349-1354.
73. N.C. Parson and T. Sheppard, "Extrusion processing of Al-Mg-Li alloys", in *Aluminium-Lithium Alloys III*, C. Baker, P.J. Gregson, S.J. Harris and C.J. Peel (eds.), The Institute of Metals, London, UK, 1986, pp. 222-232.
74. N.C. Parson and T. Sheppard, "The effect of extrusion process parameters on the microstructure and properties of an Al-Li-Mg alloy", in *Aluminum-Lithium Alloys II*, T.H. Sanders and E.A. Starke (eds.), TMS-AIME, Warrendale, PA, 1984, pp. 53-64.
75. A.K. Vasudevan, M.A. Przystupa and W.G. Fricke, "Texture-microstructure effects in yield strength anisotropy of 2090 sheet alloy", *Scripta Metall.et Mater.*, vol.24, no.8, 1990, pp. 1429-1434.
76. D. Raabe, "Microstructure and crystallographic texture of strip-cast and hot-rolled austenitic stainless steel", *Metall.& Mater.Trans. A*, vol.26A, no.4, 1995, pp. 991-998.
77. J.F. Kenney, *Mathematics of Statistics*, D. Van Nostrand Company, Inc., NY, 1939, pp. 104-107.

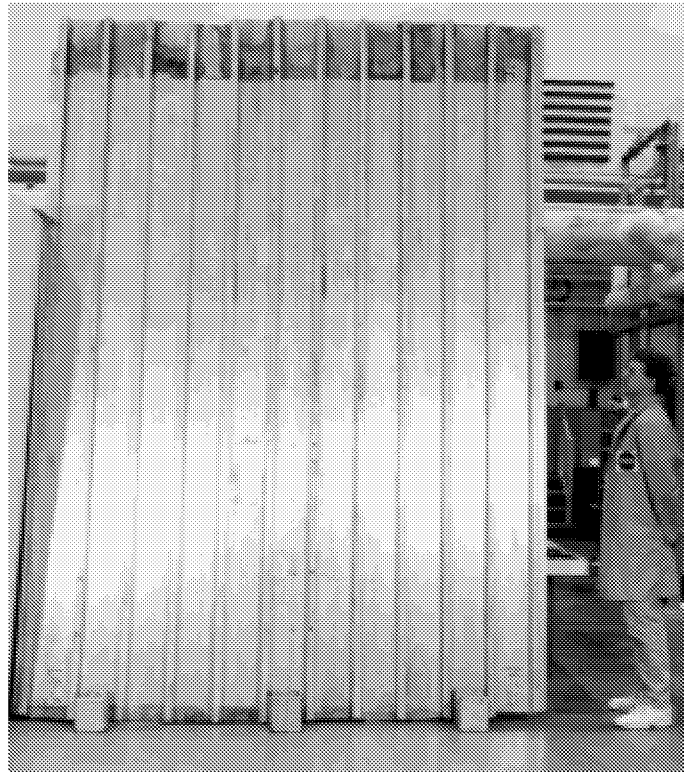


Constraint	Model	$\epsilon_{RA}$	$\epsilon_{RC}$	$\epsilon_{CA}$	$\epsilon_{CC}$	Active Slip Systems
Full (F)	F	0	0	0	0	5
Relaxed (R)	C	$\neq 0$	0	0	0	4
	S	0	$\neq 0$	0	0	4
	B	0	0	$\neq 0$	0	4
	SC	$\neq 0$	$\neq 0$	0	0	3
	BS	0	$\neq 0$	$\neq 0$	0	3
	BC	$\neq 0$	0	$\neq 0$	0	3
	BSC	$\neq 0$	$\neq 0$	$\neq 0$	0	2
No (N)	N	$\neq 0$	$\neq 0$	$\neq 0$	$\neq 0$	1

Figure 1. Taylor-type models, ranked by decreasing levels of constraint from the Taylor model, through various Relaxed Constraint models, to the Sachs model, where  $\epsilon_{xy}$  refers to shear on the plane perpendicular to the X direction in the Y direction and  $\epsilon_{cc}$  is the Poisson effect.



(a) Original cylindrical cross-section with stiffeners on the outer surface



(b) Flattened panel following secondary processing

Figure 2. Photographs of the extrusions.

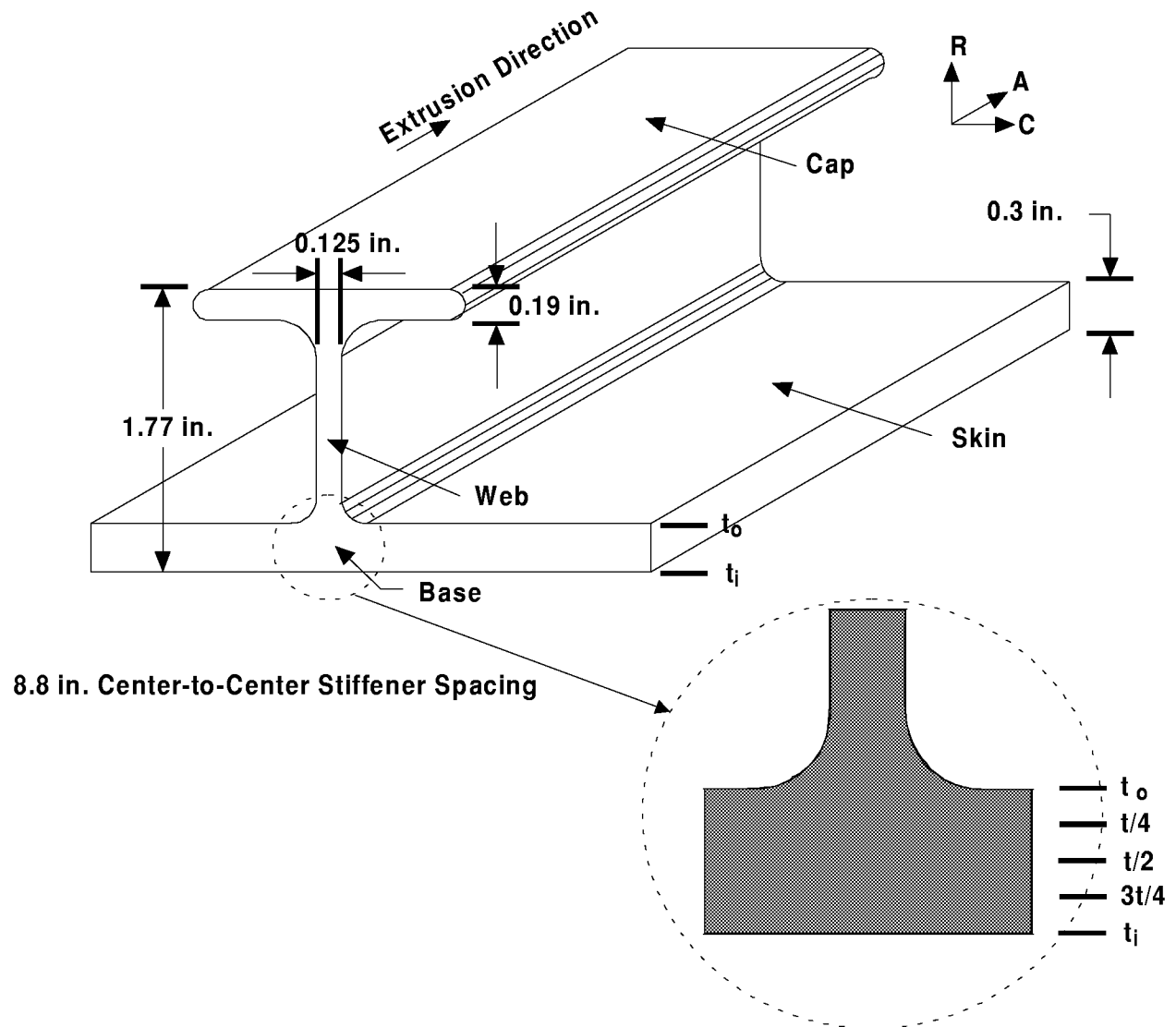


Figure 3. Extrusion schematic showing cross-sectional geometry, dimensions and nomenclature adopted; (A)xial, (R)adial, (C)ircumferential.

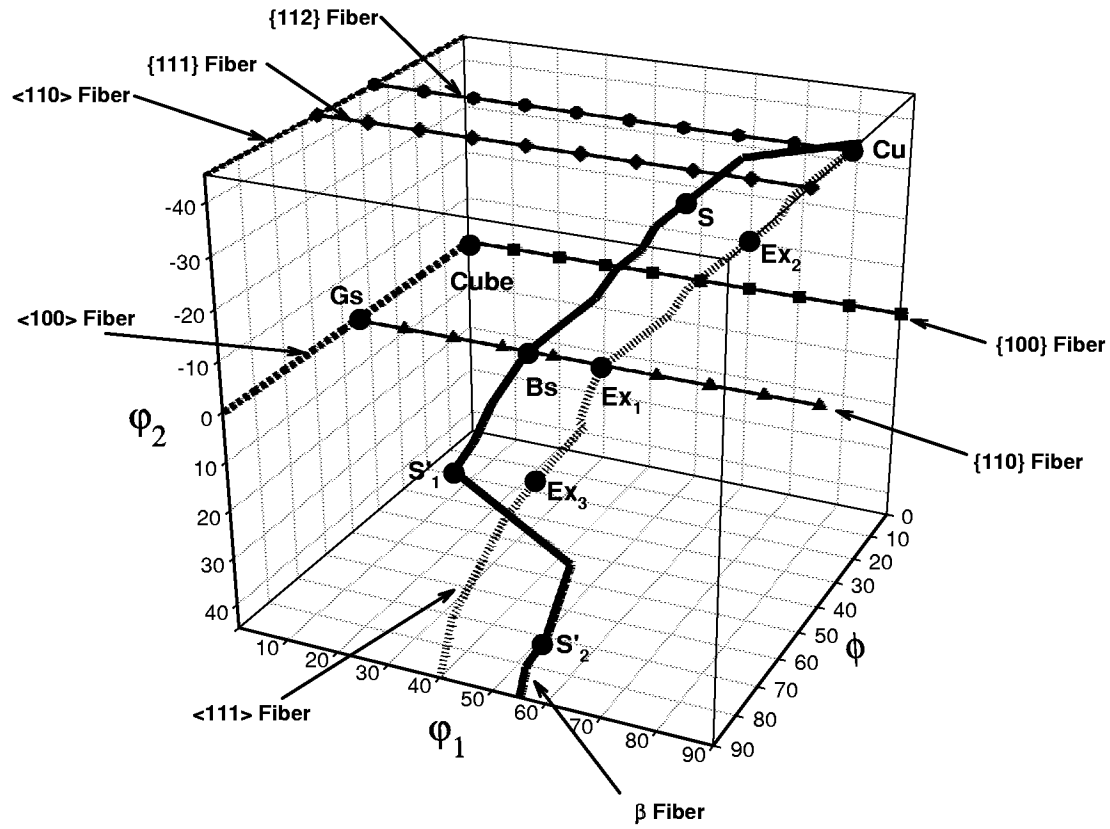
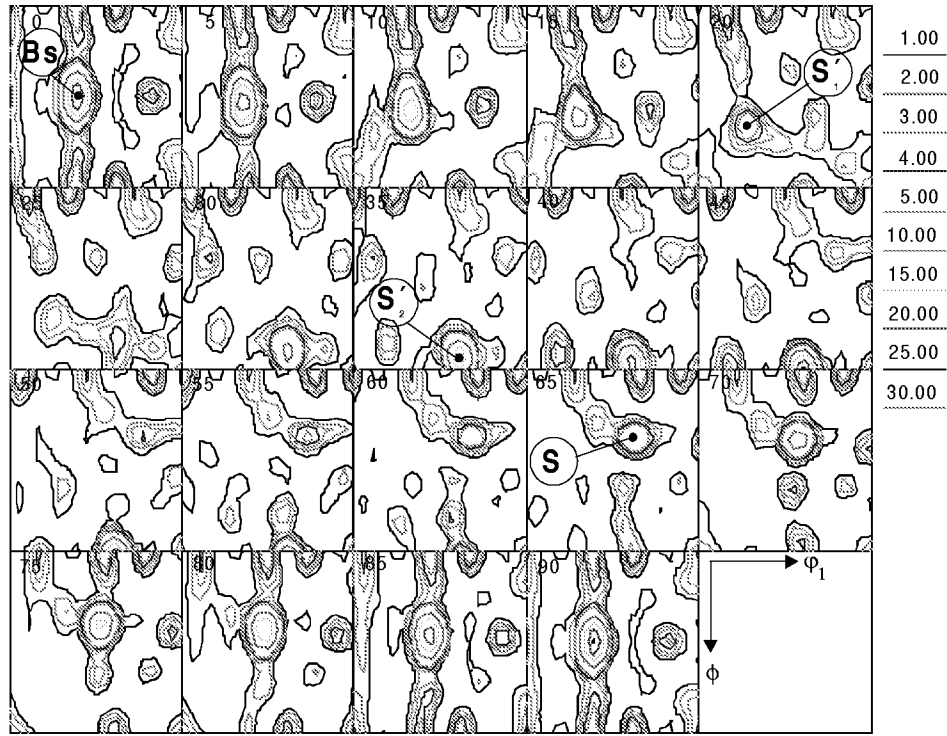
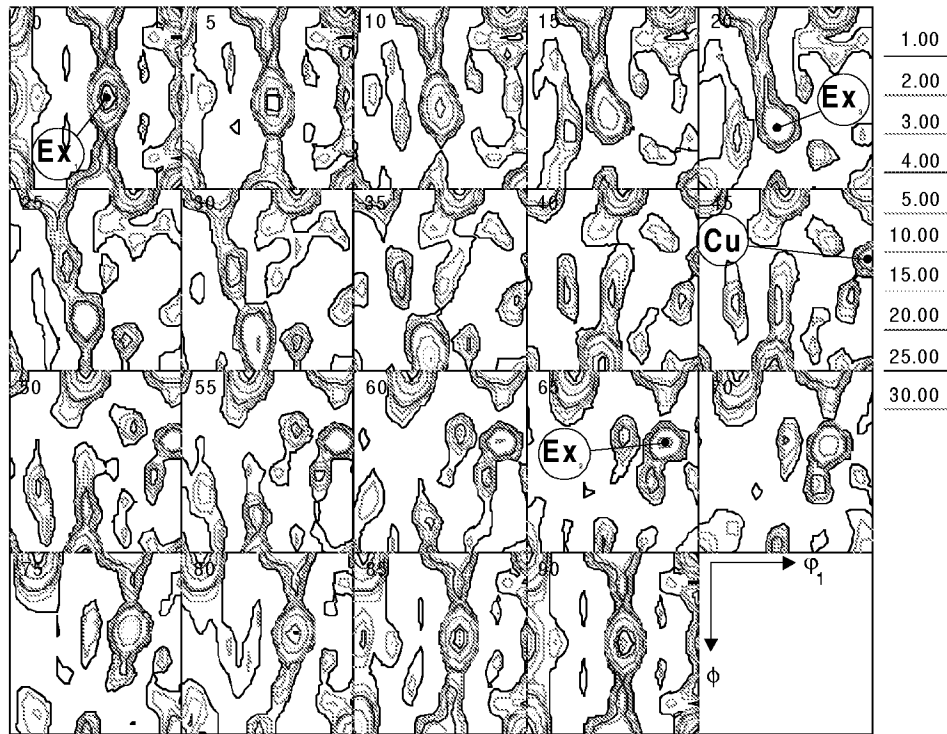


Figure 4. 3-D schematic of texture fibers, using Bunge notation[26], illustrating the relative positions of common  $\{hkl\}$  and  $\langle uvw \rangle$  fibers found in Al alloys in Euler space.

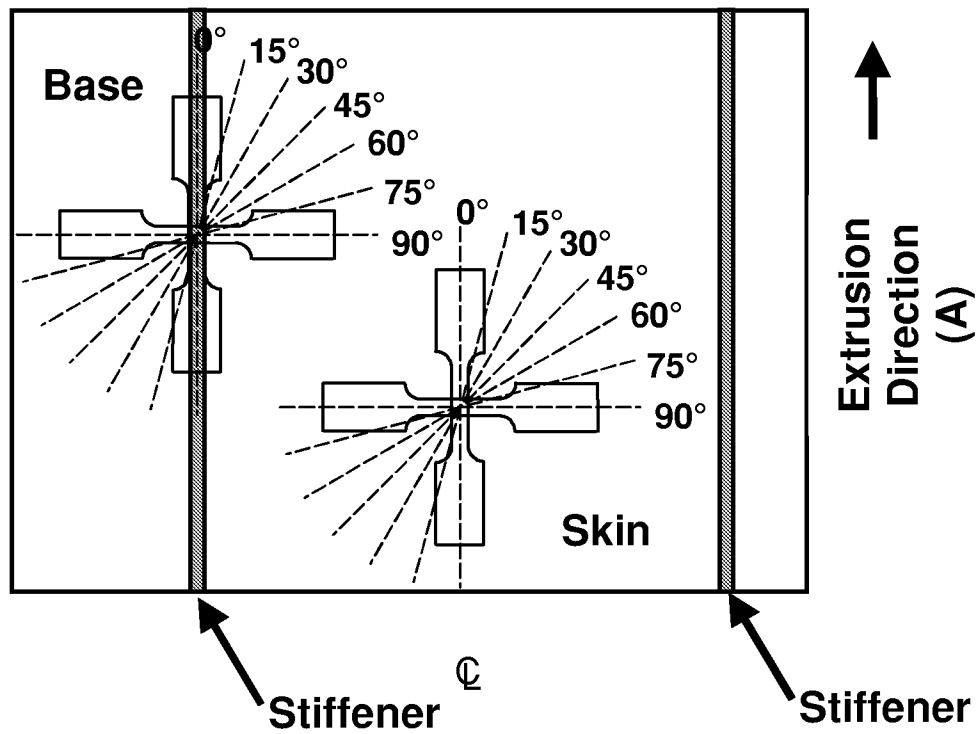


(a) 2098 Skin at  $t/2$

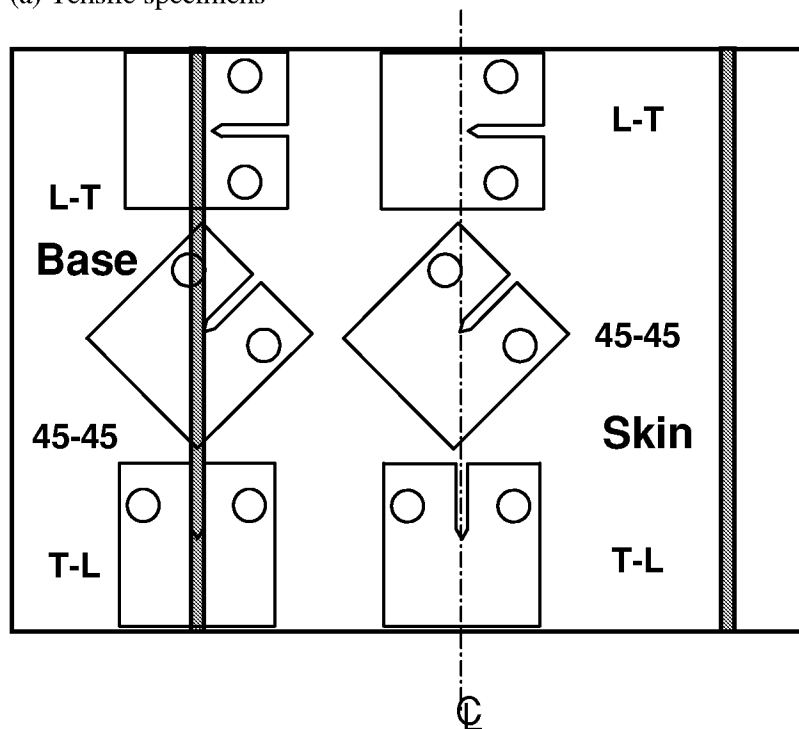


(b) 2098 Base at  $t/2$

Figure 5. Typical ODF data, all  $\phi_2$  sections.



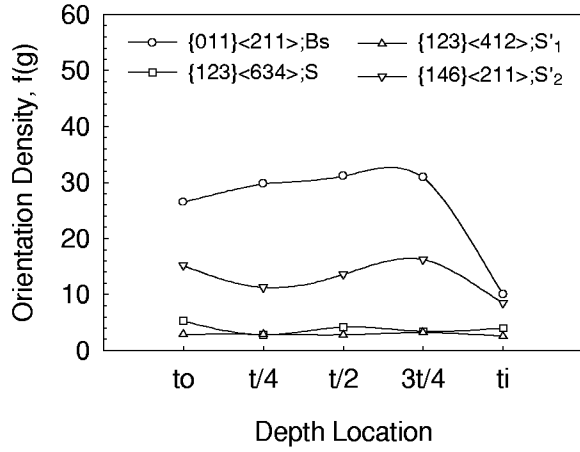
(a) Tensile specimens



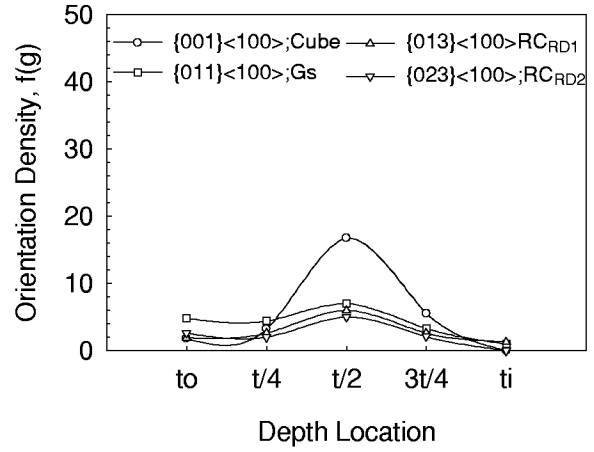
(b) Fracture toughness specimens

Figure 6. Mechanical test specimen schematic, showing the location and orientation of specimens machined from the extrusions in the Skin and Base regions.

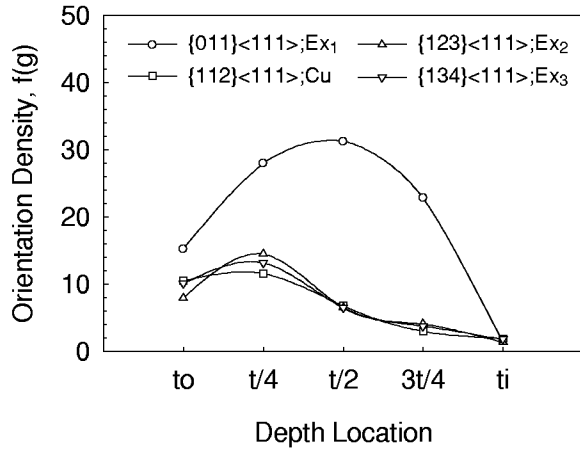




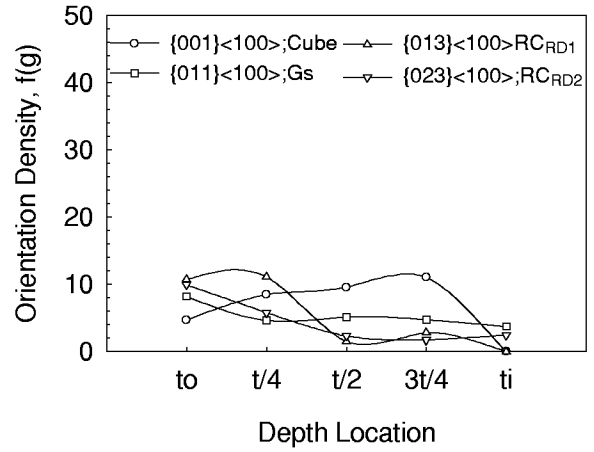
(a) Skin DF components as  $f(t)$



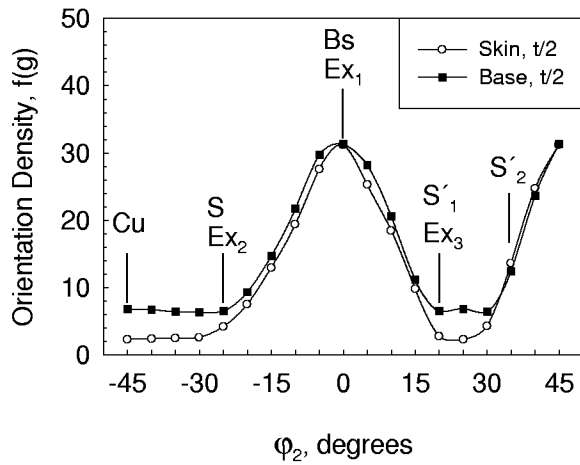
(b) Skin RX components as  $f(t)$



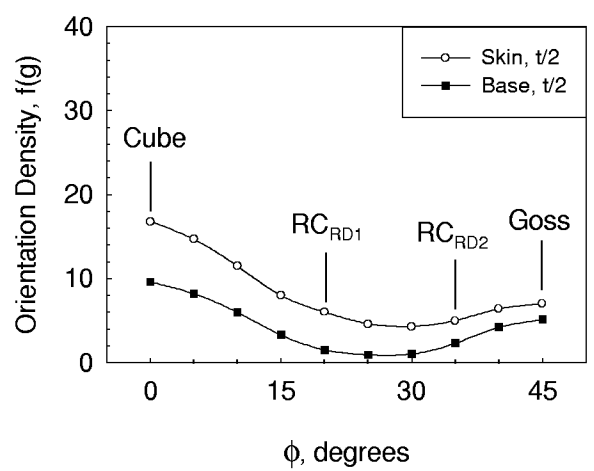
(c) Base DF components as  $f(t)$



(d) Base RX components as  $f(t)$

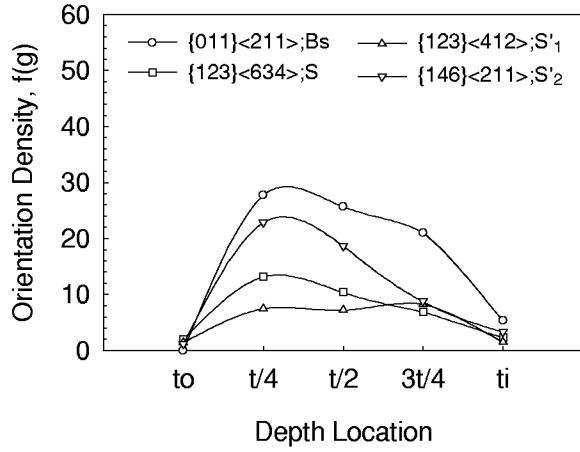


(e) Skin-Base DF fibers as  $f(\phi_2)$  @  $t/2$

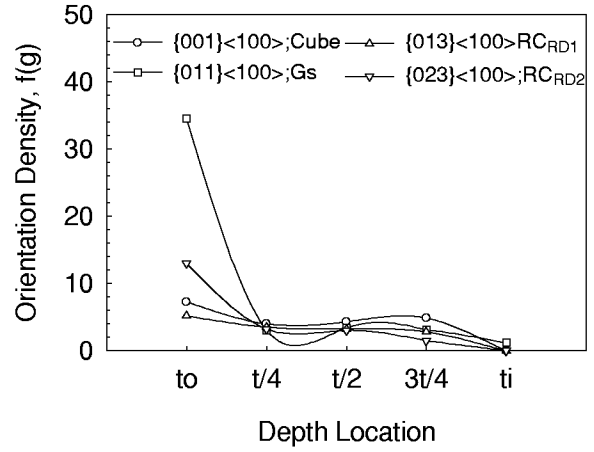


(f) Skin-Base RX fibers as  $f(\phi)$  at  $t/2$

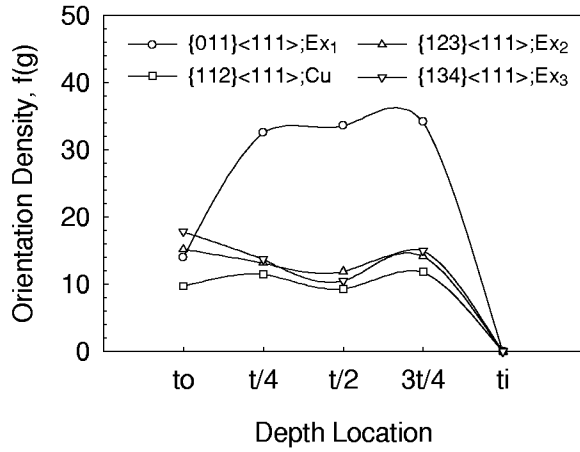
Figure 7. 2195 texture characteristics.



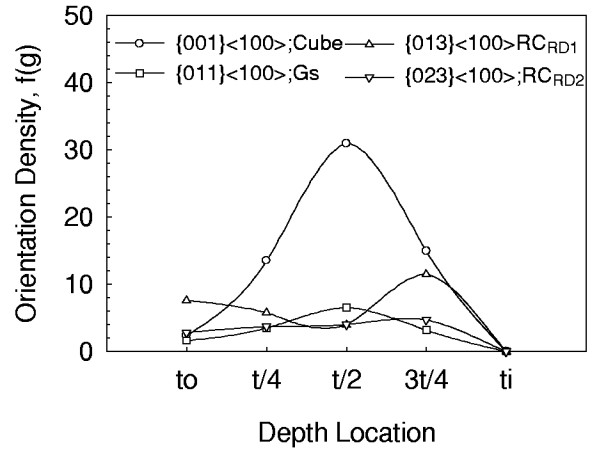
(a) Skin DF components as  $f(t)$



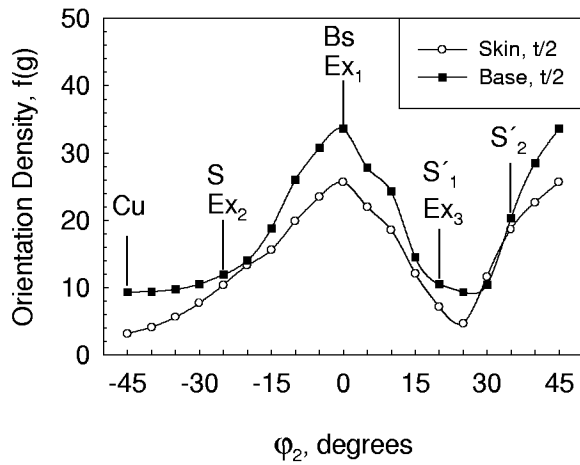
(b) Skin RX components as  $f(t)$



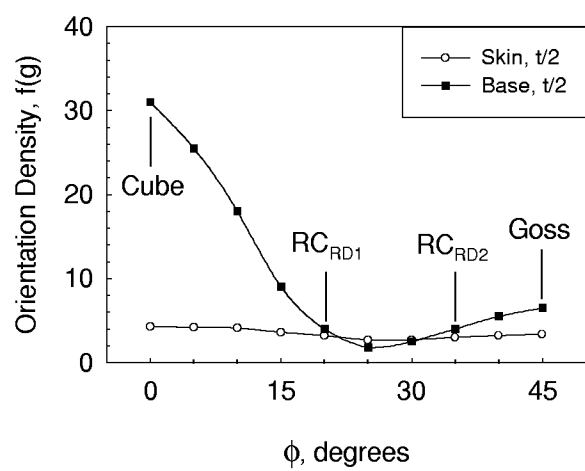
(c) Base DF components as  $f(t)$



(d) Base RX components as  $f(t)$

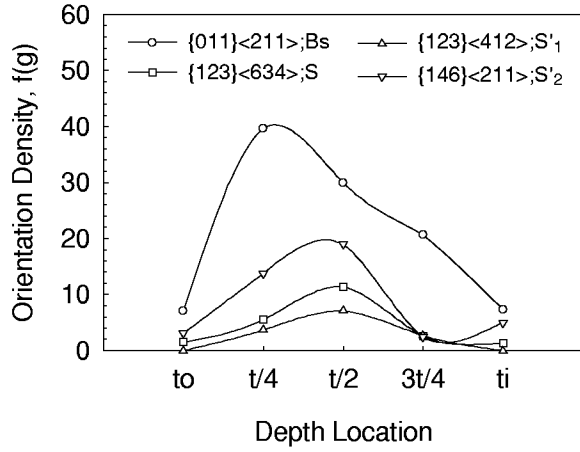


(e) Skin-Base DF fibers as  $f(\phi_2)$  @  $t/2$

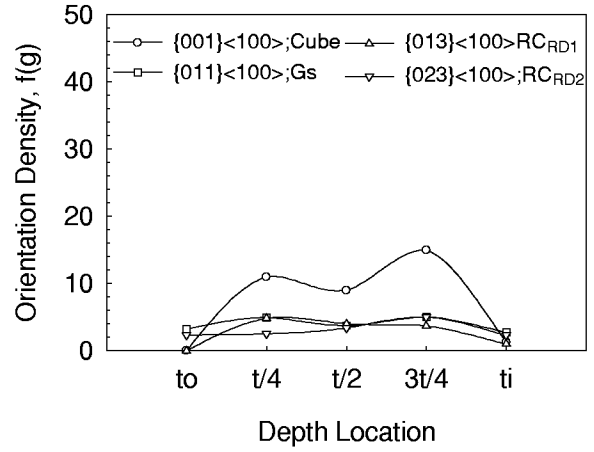


(f) Skin-Base RX fibers as  $f(\phi)$  at  $t/2$

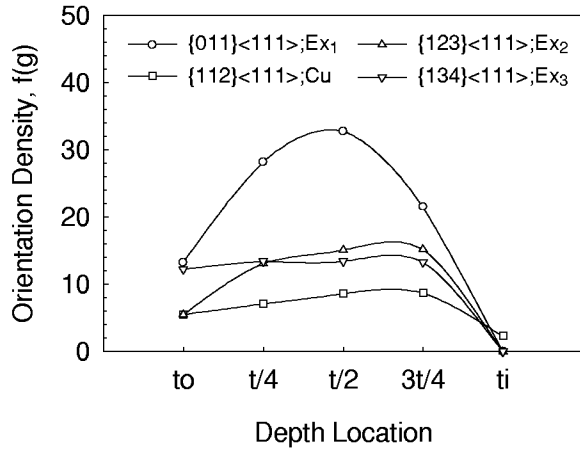
Figure 8. 2098 texture characteristics.



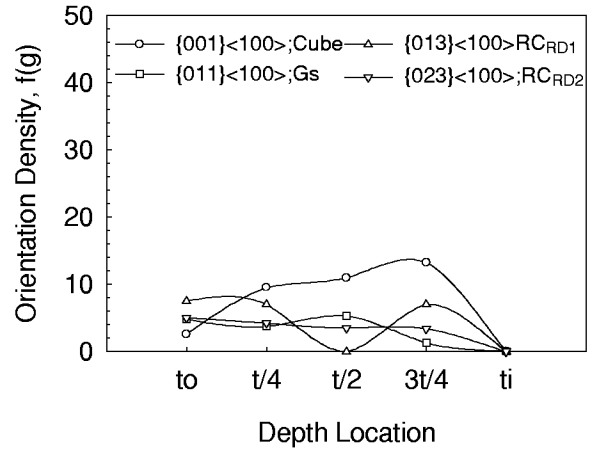
(a) Skin DF components as  $f(t)$



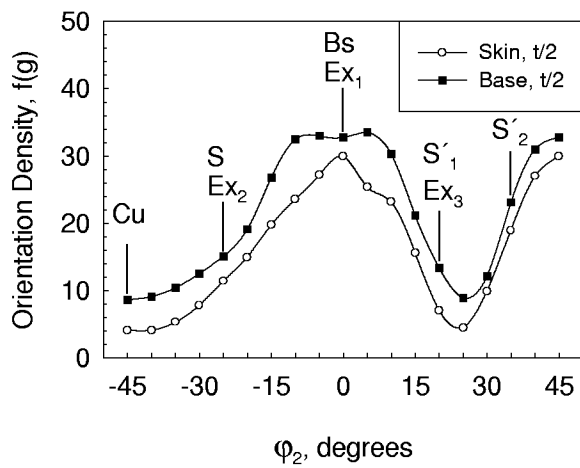
(b) Skin RX components as  $f(t)$



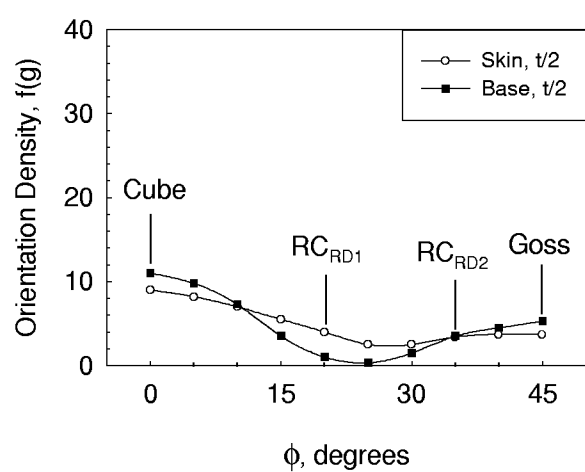
(c) Base DF components as  $f(t)$



(d) Base RX components as  $f(t)$



(e) Skin-Base DF fibers as  $f(\phi_2)$  @  $t/2$



(f) Skin-Base RX fibers as  $f(\phi)$  at  $t/2$

Figure 9. 2096 texture characteristics.

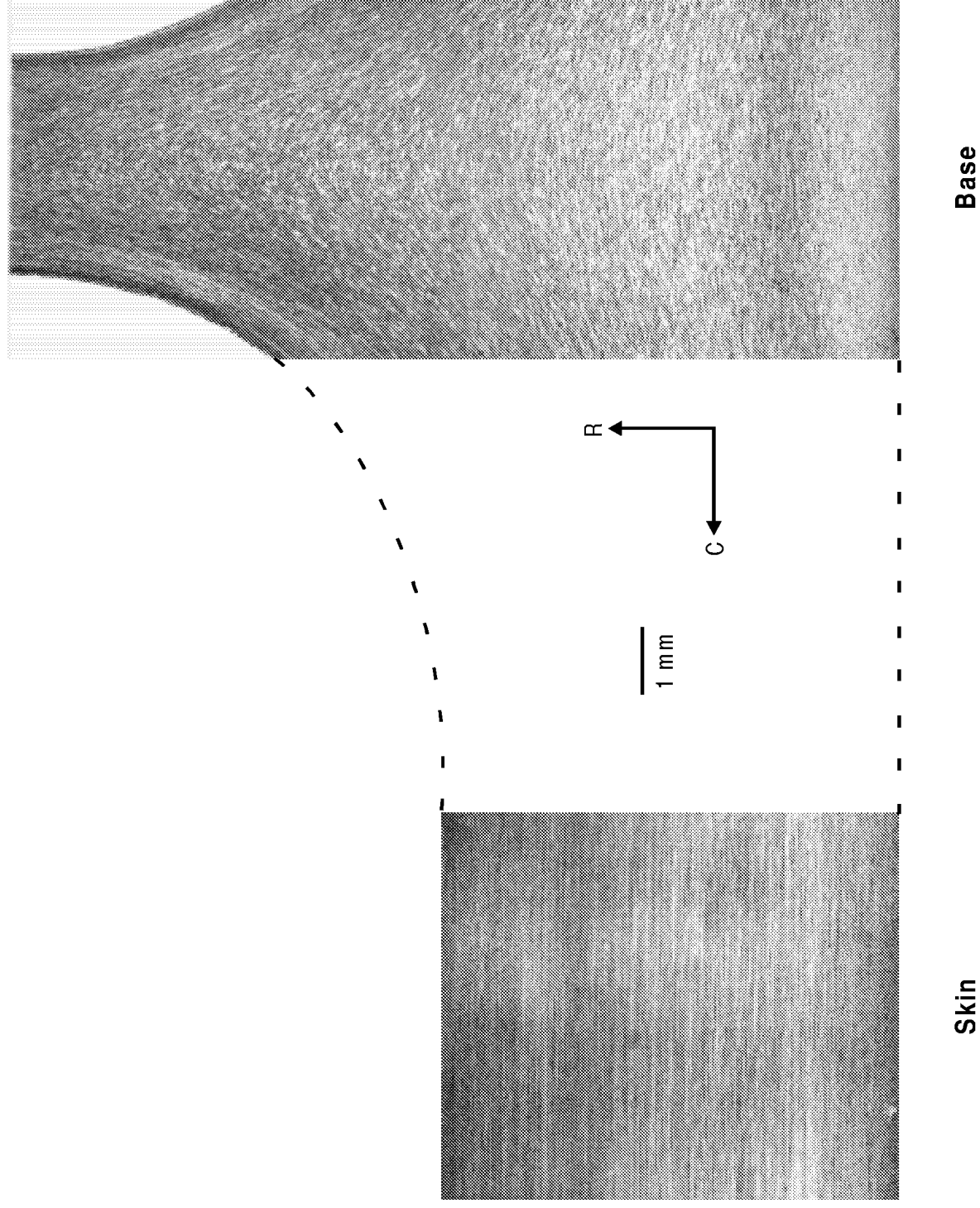


Figure 10. 2195 macrostructural characteristics; Nomarski contrast images; R-C plane; Skin and Base regions.

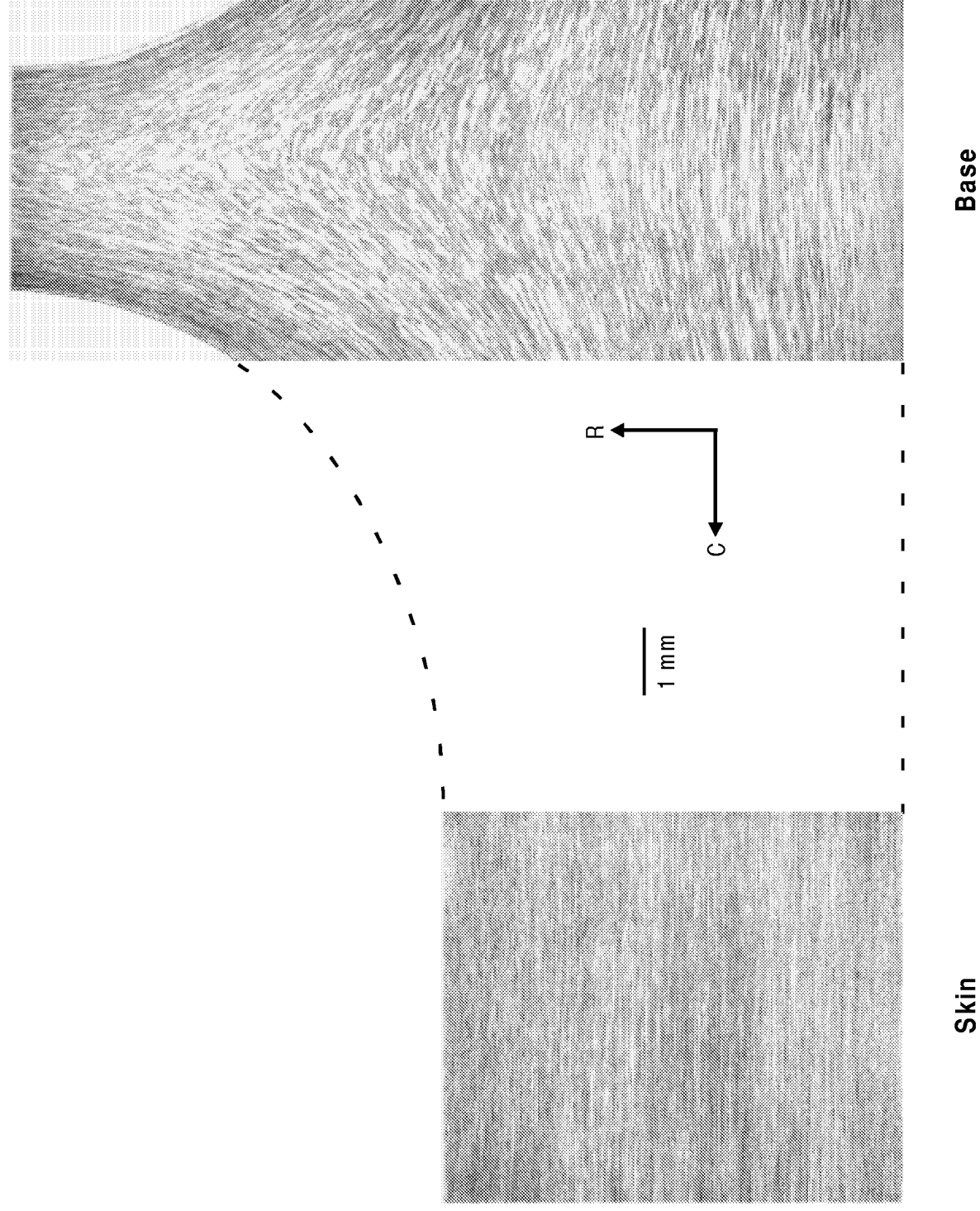
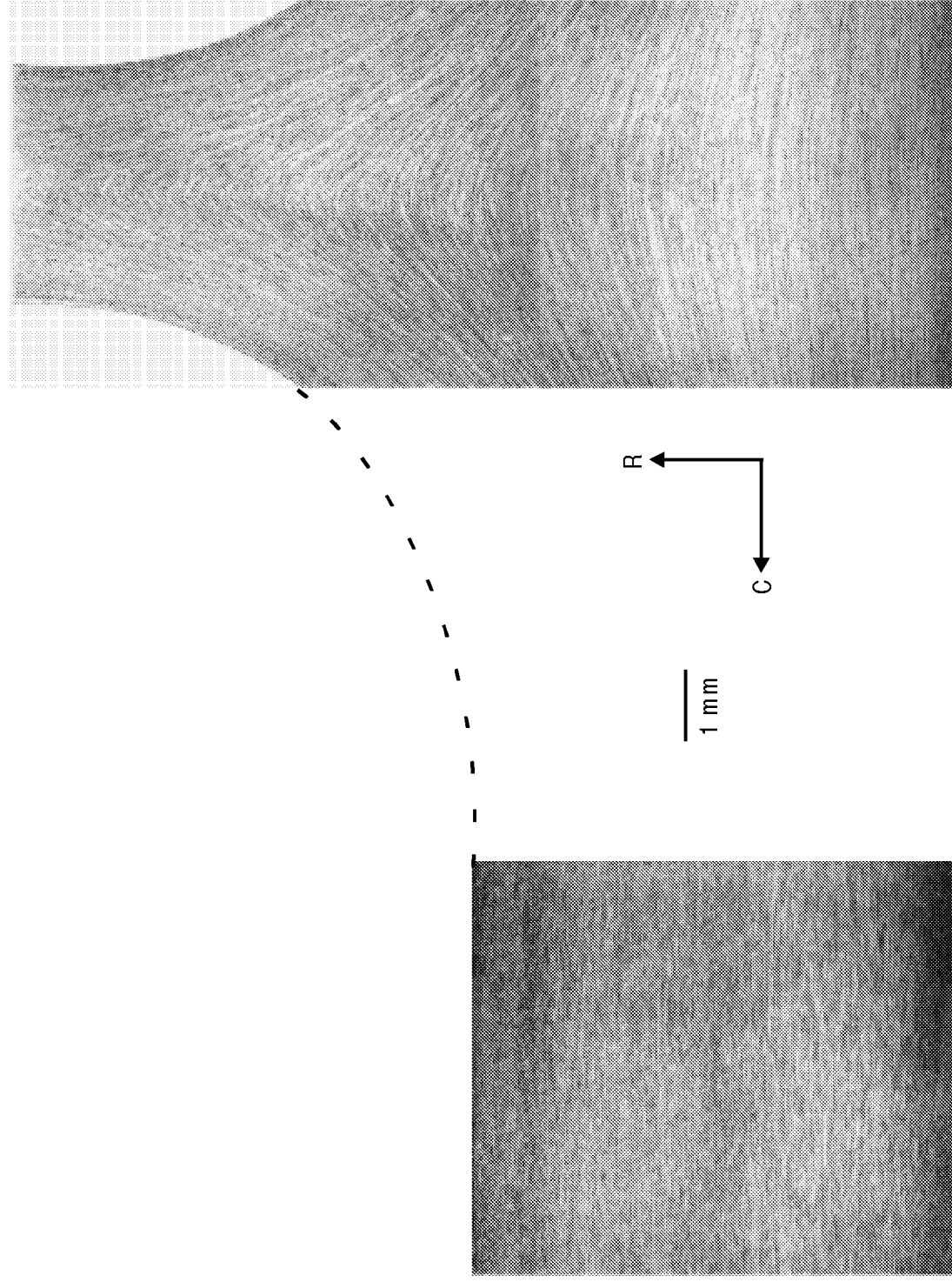
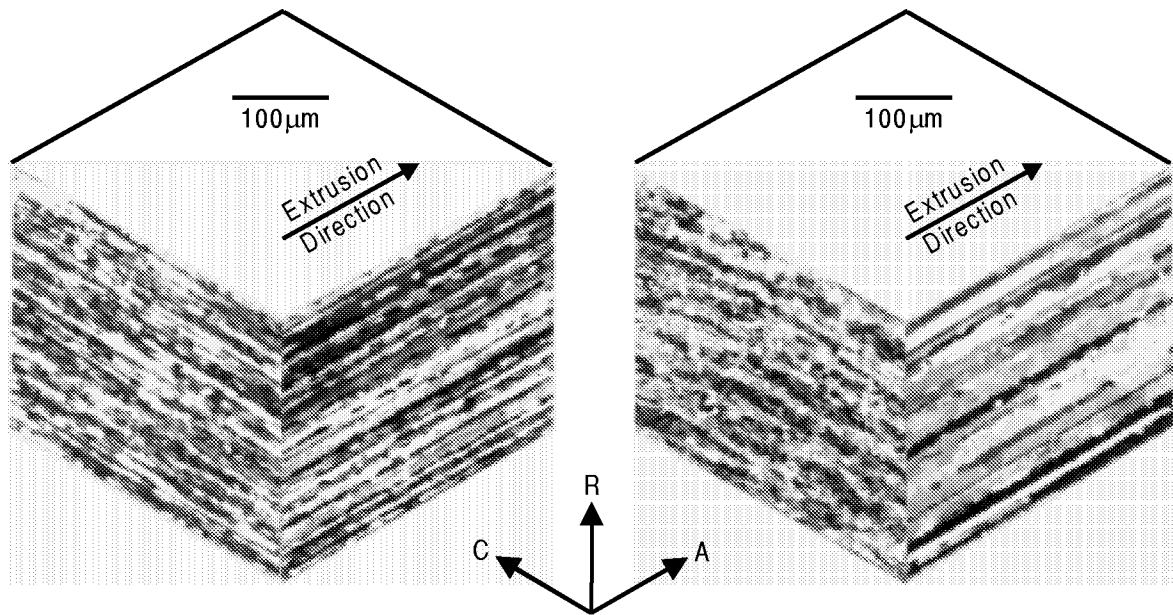


Figure 11. 2098 macrostructural characteristics; Nomarski contrast images; R-C plane; Skin and Base regions.



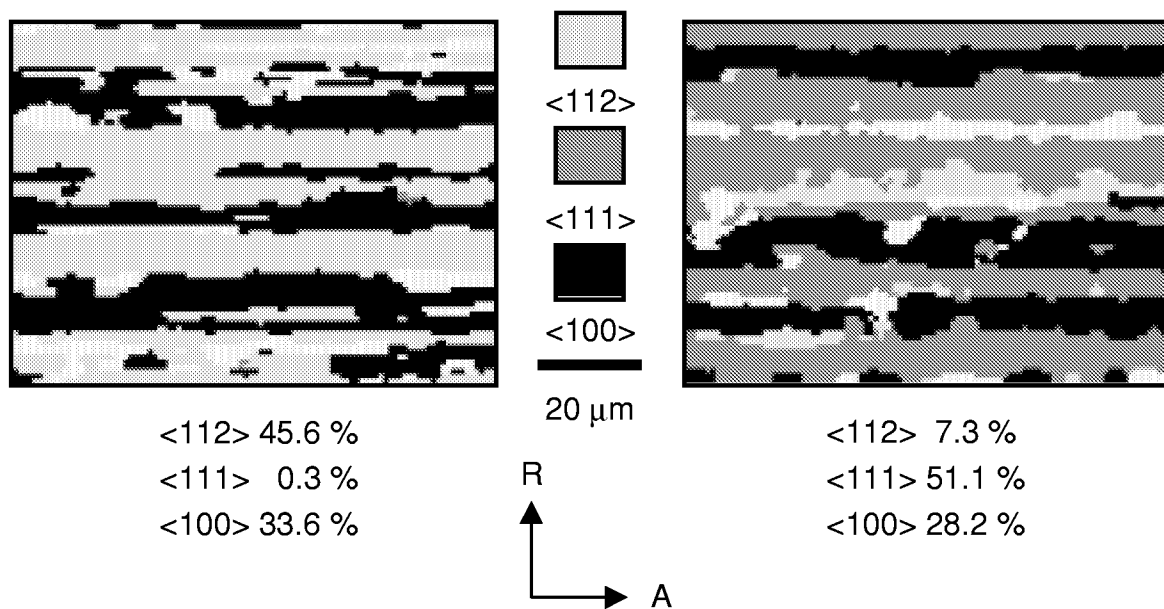
**Skin** **Base**

Figure 12. 2096 macrostructural characteristics; Nomarski contrast images; R-C plane; Skin and Base regions.



(a) Skin, C-R/A-R planes

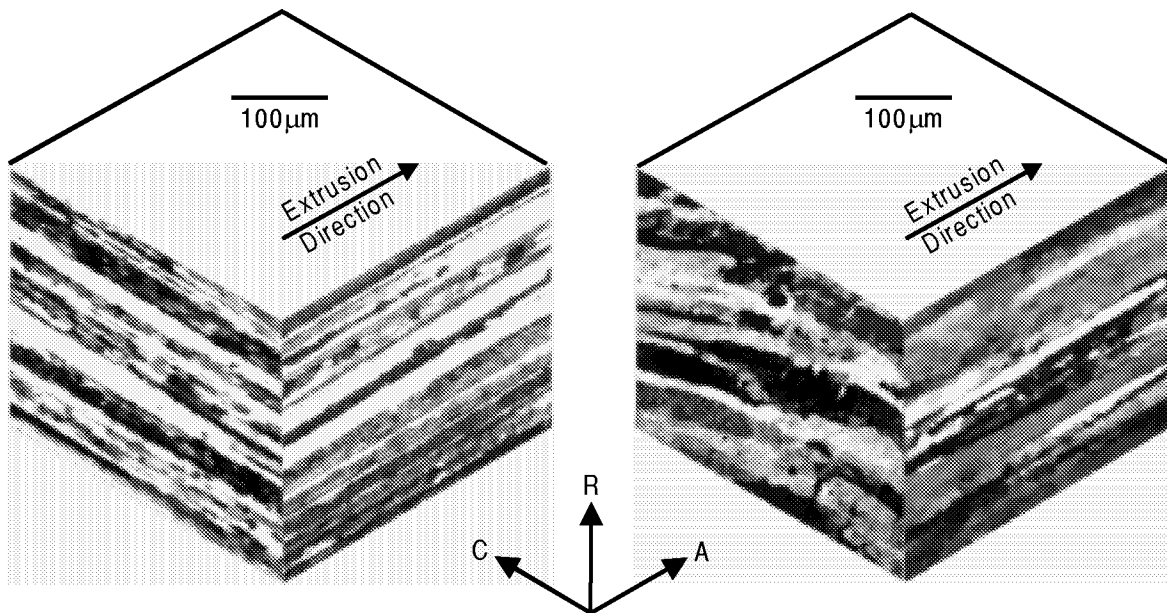
(b) Base, C-R/A-R planes



(c) Skin microtexture A-R plane

(d) Base microtexture A-R plane.

Figure 13. 2195 microstructural and microtextural characteristics at  $t/2$ .



(a) Skin, C-R/A-R planes

(b) Base, C-R/A-R planes

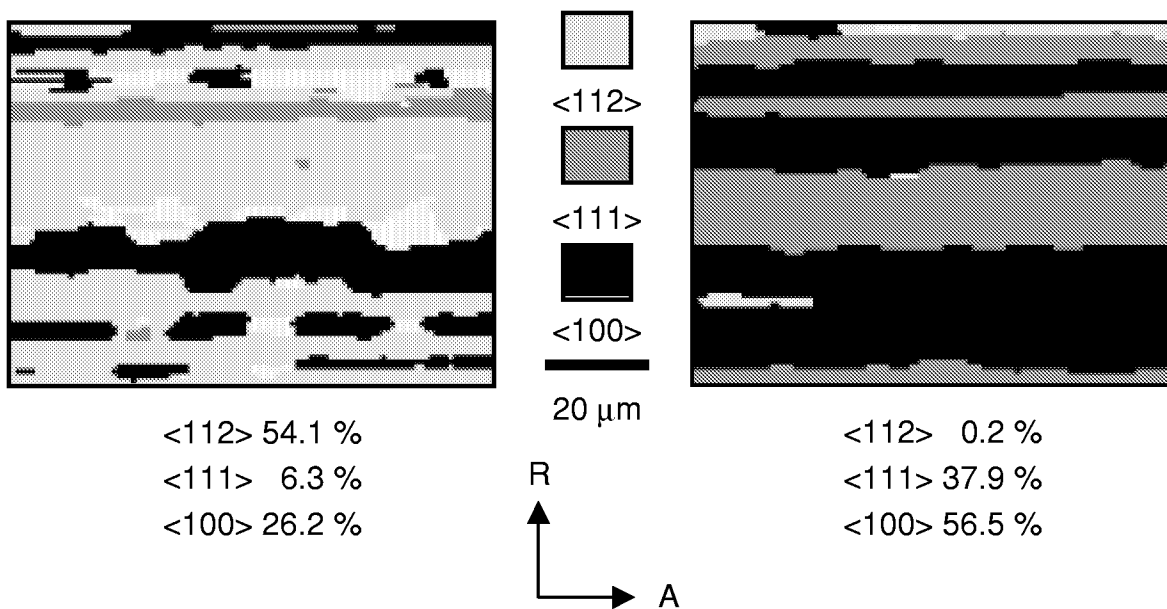
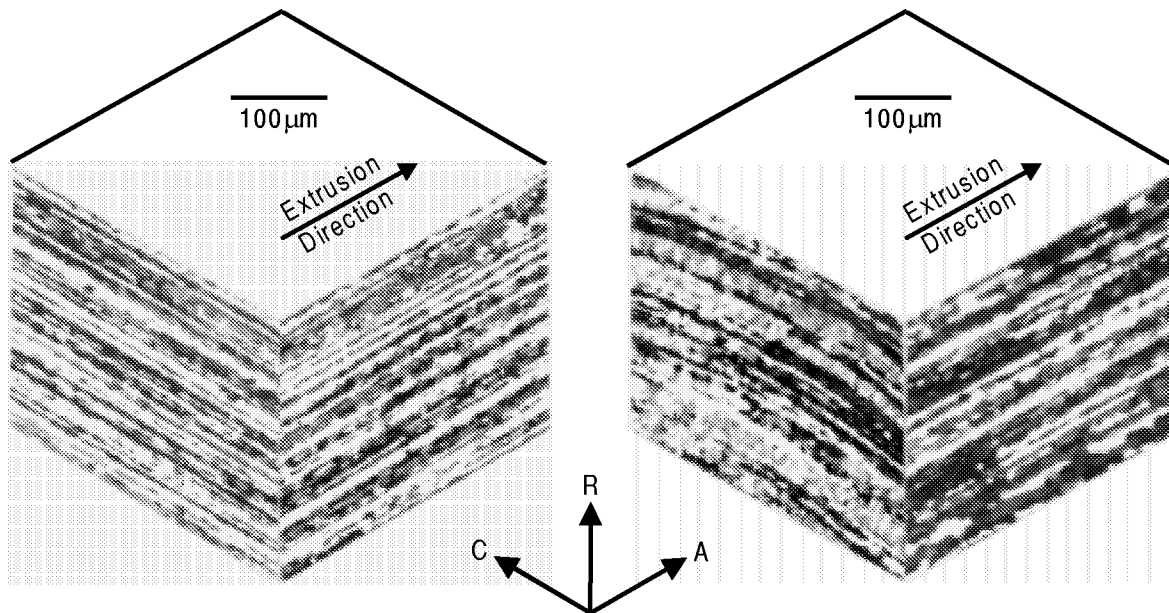


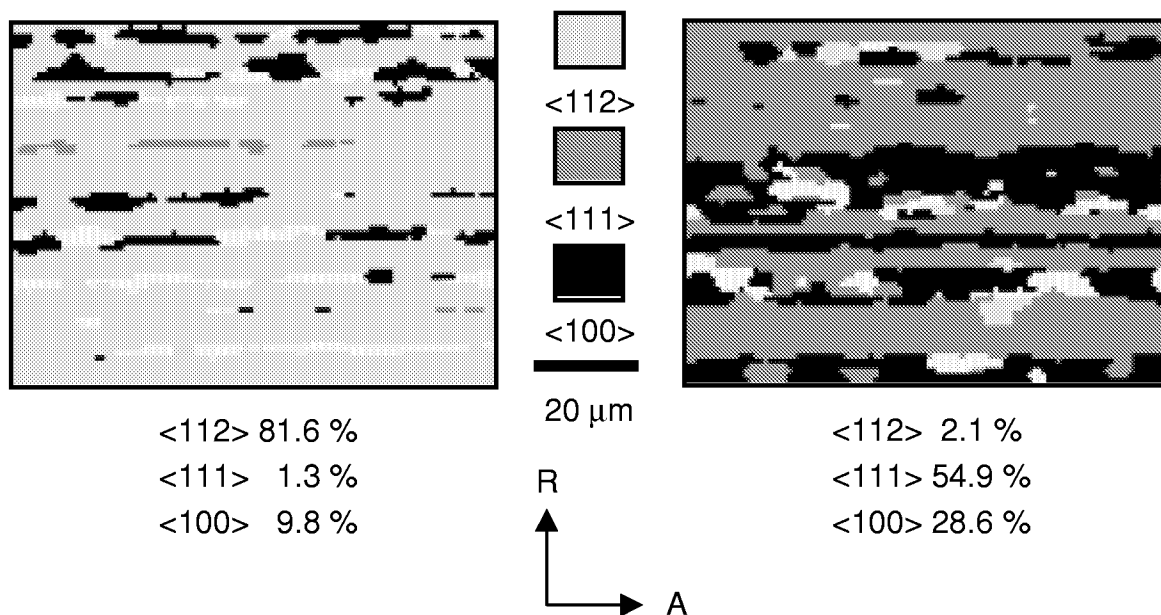
Figure 14. 2098 microstructural and microtextural characteristics at  $t/2$ .





(a) Skin, C-R/A-R planes

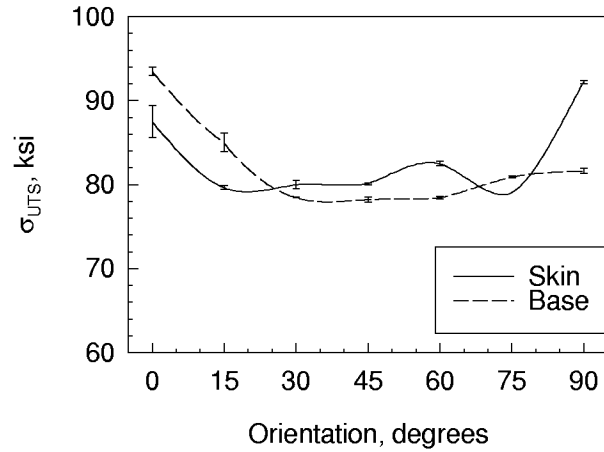
(b) Base, C-R/A-R planes



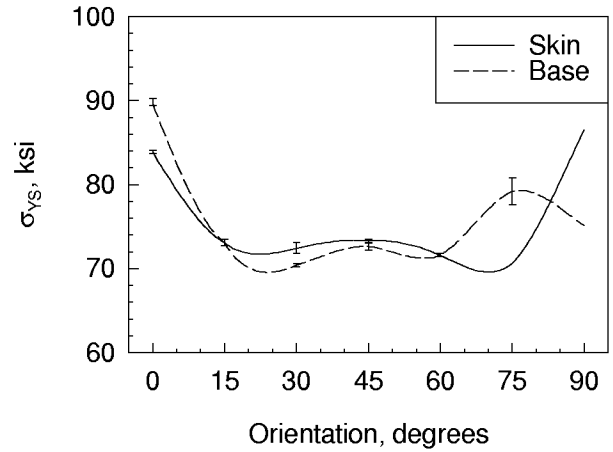
(c) Skin microtexture A-R plane

(d) Base microtexture A-R plane.

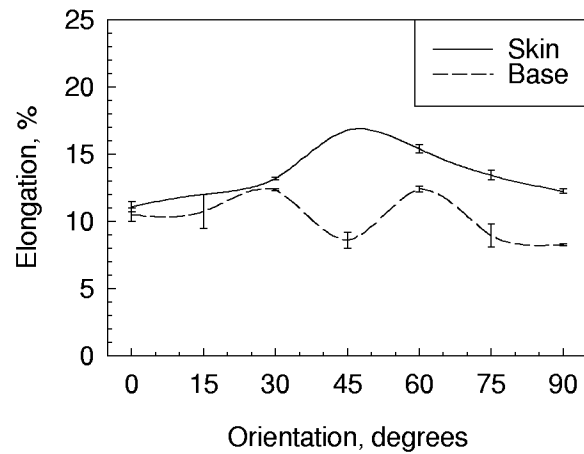
Figure 15. 2096 microstructural and microtextural characteristics at  $t/2$ .



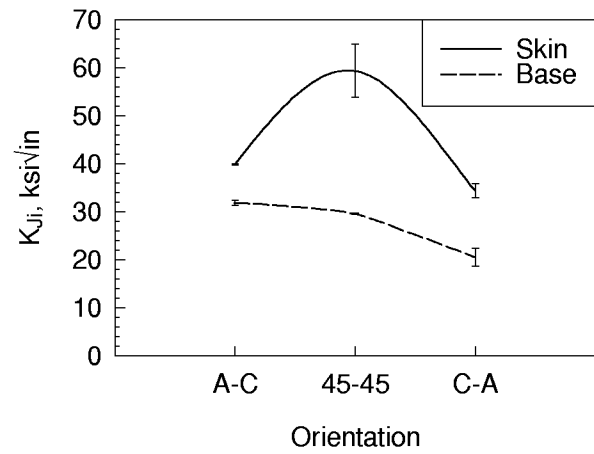
(a) Ultimate tensile strength vs. orientation



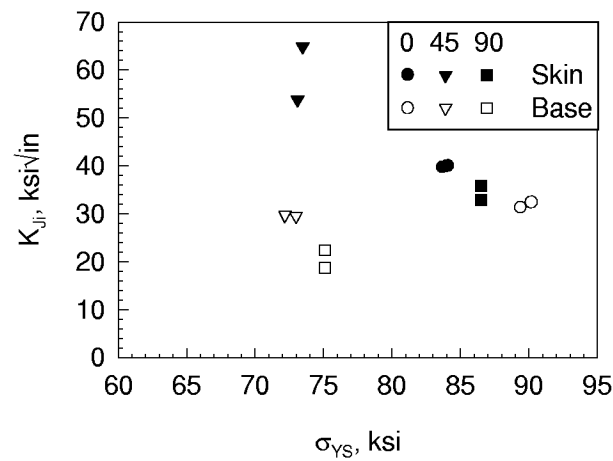
(b) Yield strength vs. orientation



(c) Elongation vs. orientation

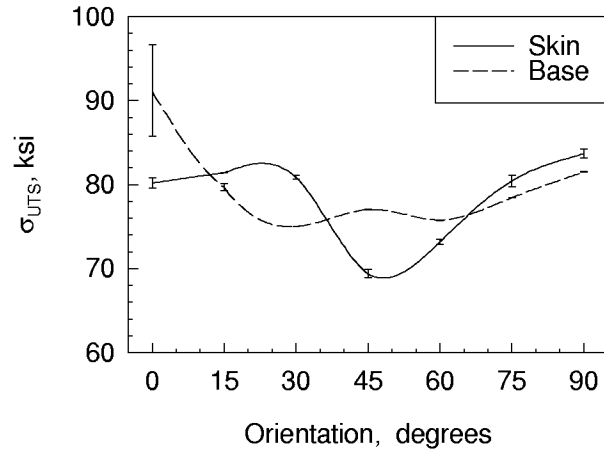


(d) Initiation toughness vs. orientation

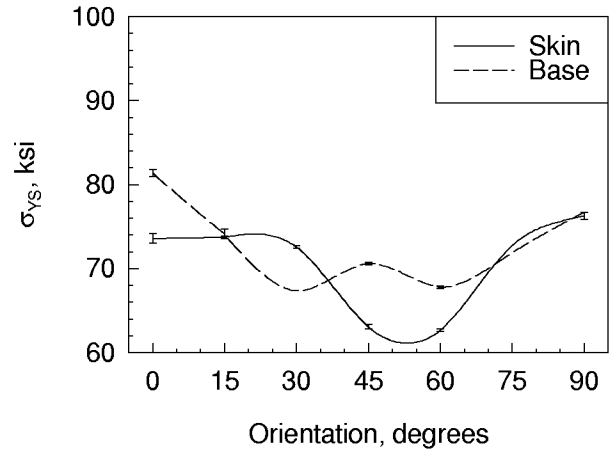


(e) Initiation toughness vs. yield strength.

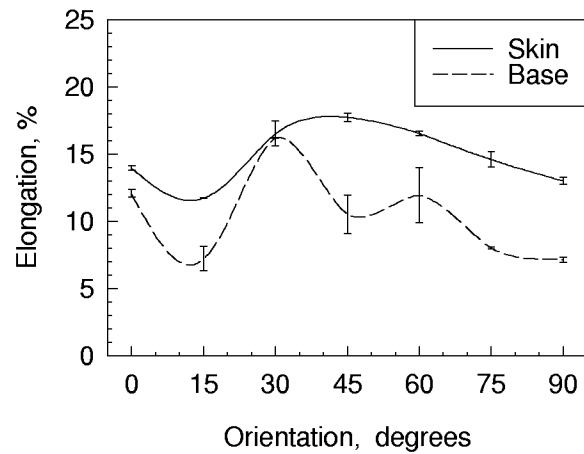
Figure 16. 2195 mechanical properties in Skin and Base, data includes range bars.



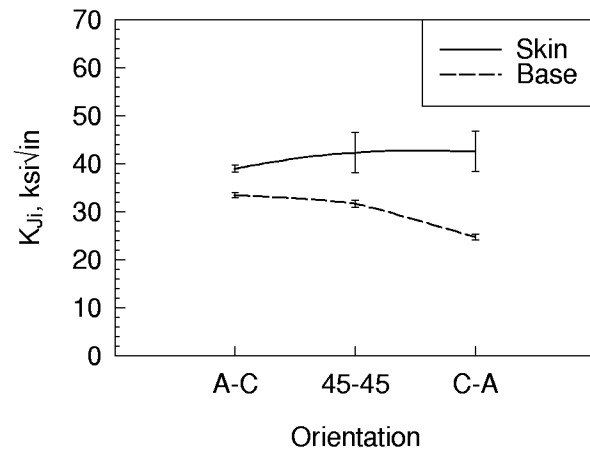
(a) Ultimate tensile strength vs. orientation



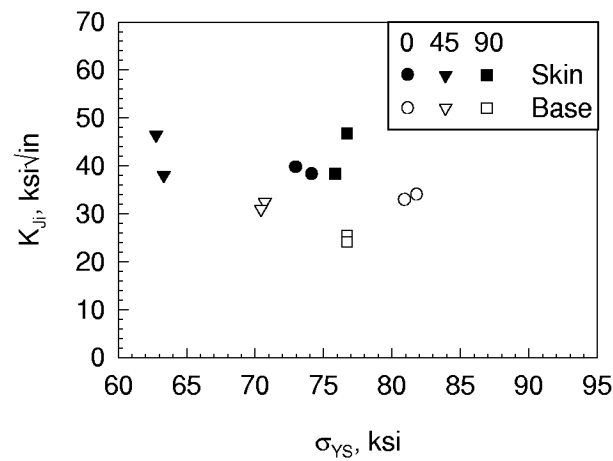
(b) Yield strength vs. orientation



(c) Elongation vs. orientation

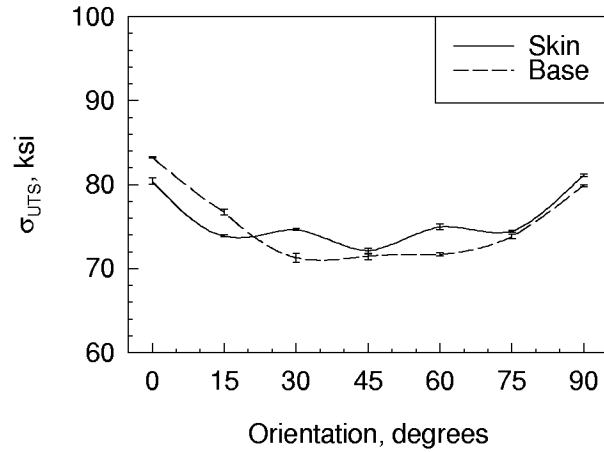


(d) Initiation toughness vs. orientation

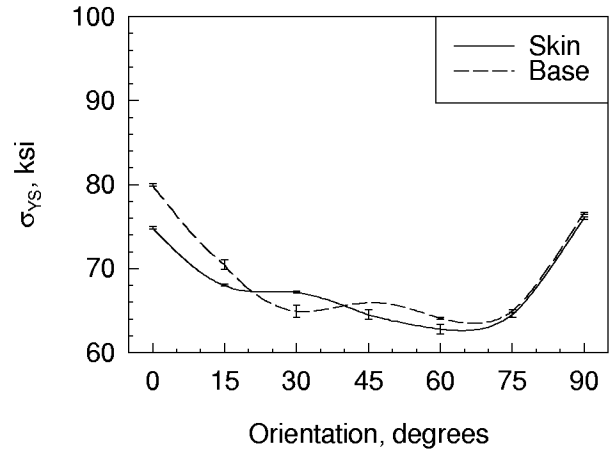


(e) Initiation toughness vs. yield strength

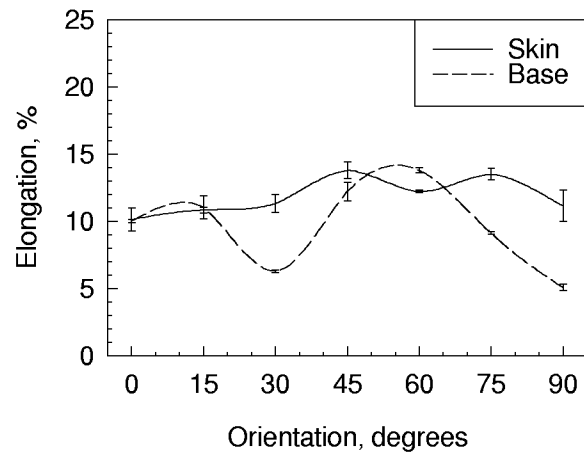
Figure 17. 2098 mechanical properties in Skin and Base, data includes range bars.



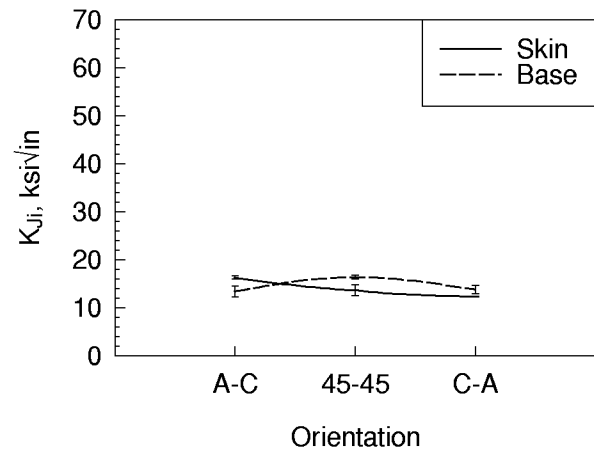
(a) Ultimate tensile strength vs. orientation



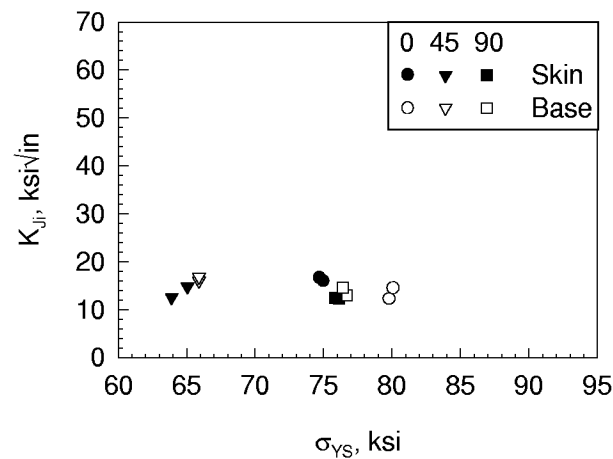
(b) Yield strength vs. orientation



(c) Elongation vs. orientation

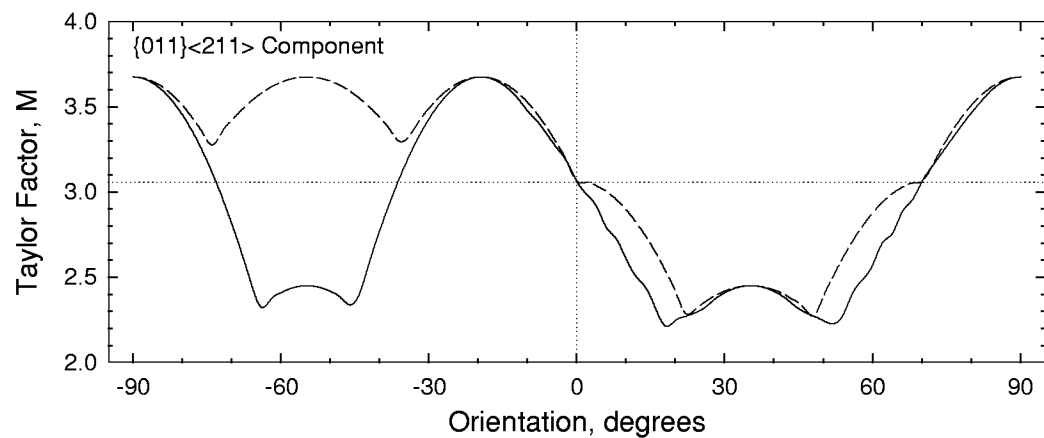


(d) Initiation toughness vs. orientation

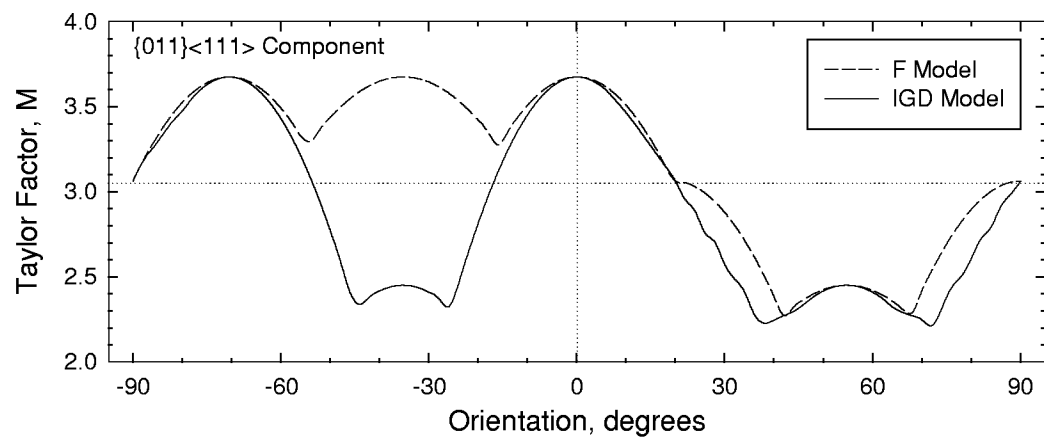


(e) Initiation toughness vs. yield strength

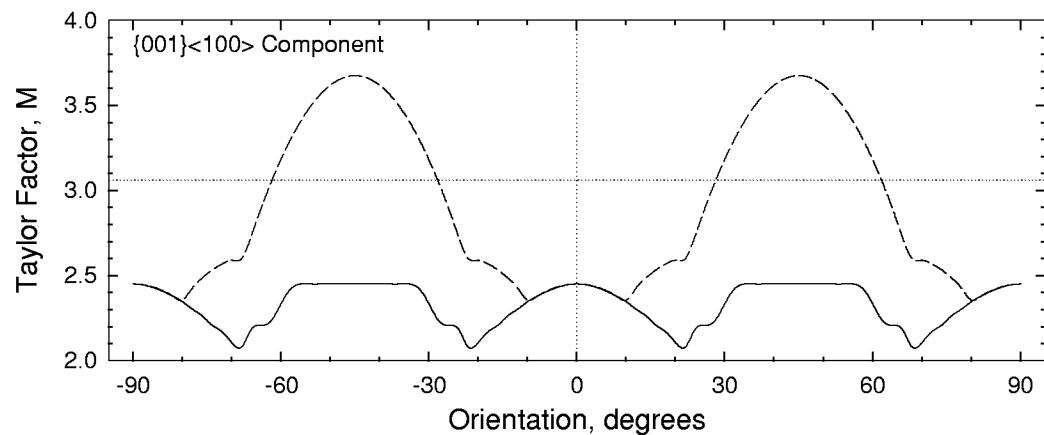
Figure 18. 2096 mechanical properties in Skin and Base, data includes range bars.



(a) Brass

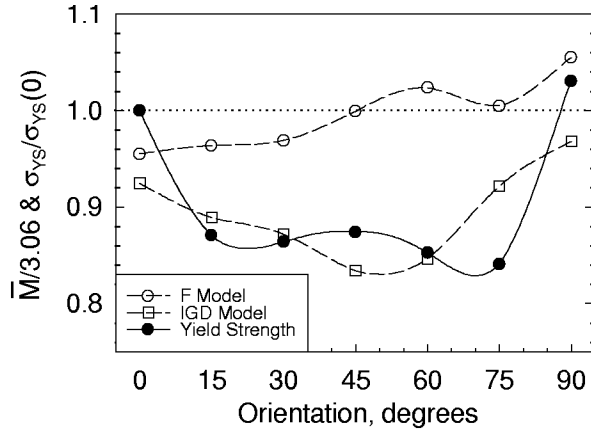


(b)  $Ex_1$

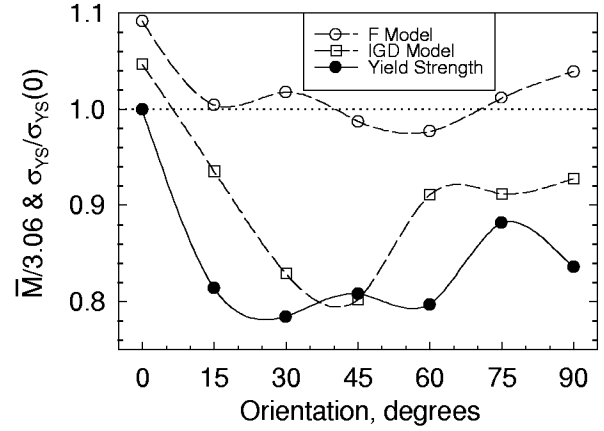


(c) Cube

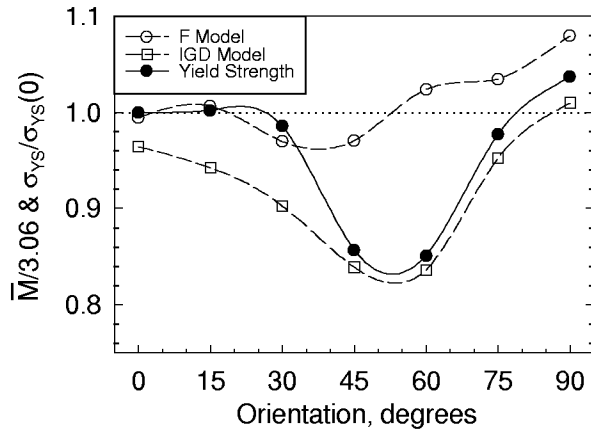
Figure 19. Taylor Factor calculations: full constraint (F) vs. relaxed constraint (IGD) models;  $-90^\circ$  to  $+90^\circ$  orientation.



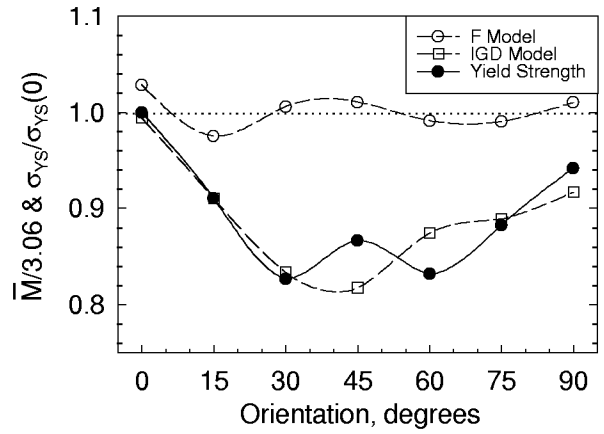
(a) 2195 Skin



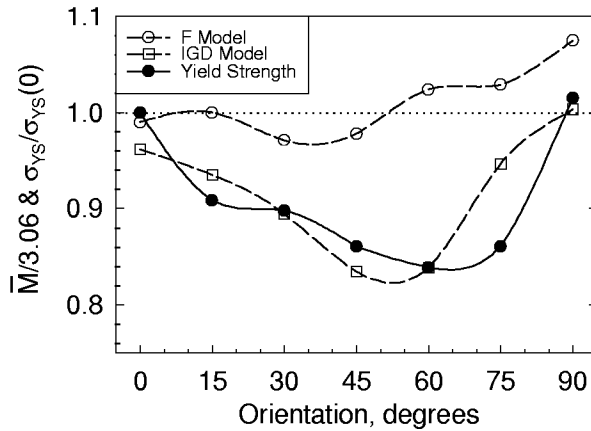
(b) 2195 Base



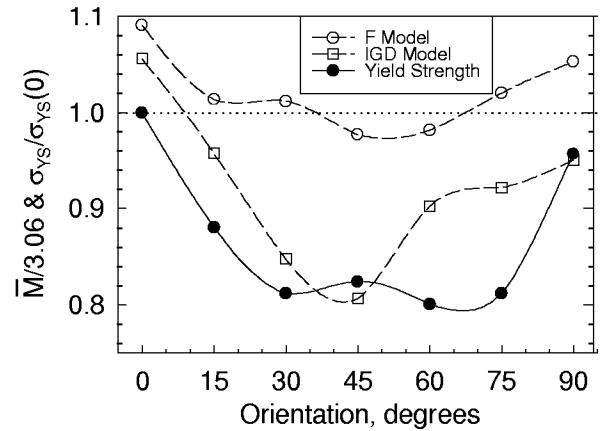
(c) 2098 Skin



(d) 2098 Base



(e) 2096 Skin

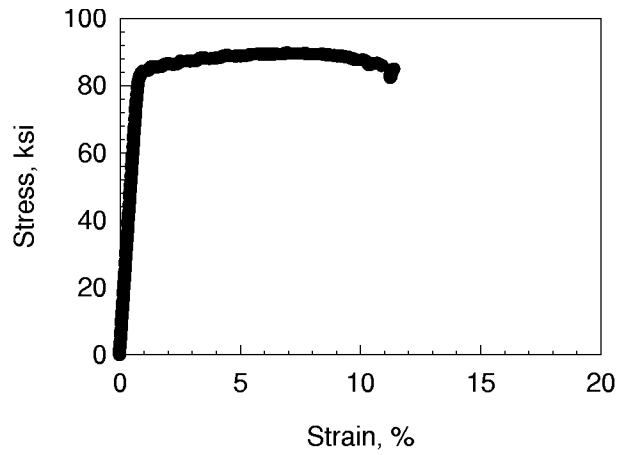


(f) 2096 Base

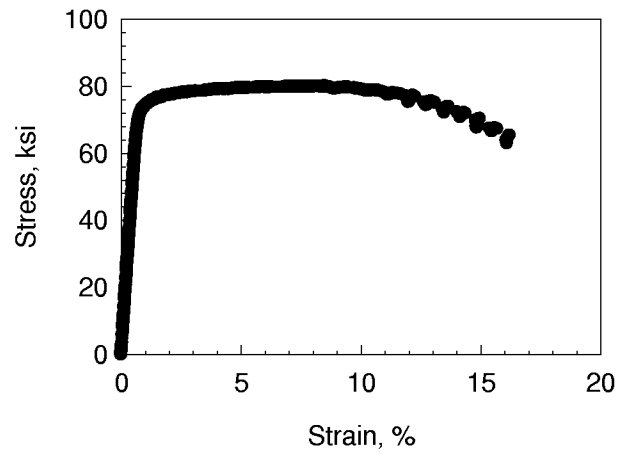
Figure 20. Normalized Taylor factor ( $\bar{M}/3.06$ ) vs. normalized yield strength ( $\sigma_{YS}/\sigma_{YS}(0)$ ) for Full constraint (F) vs. Relaxed constraint (IGD) models.

## **Appendix**

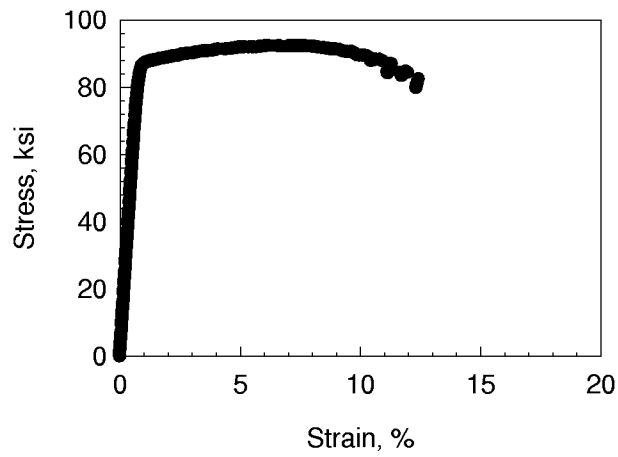
Figures A1 through A6 present typical mechanical test data for the three alloys in the Skin and Base.



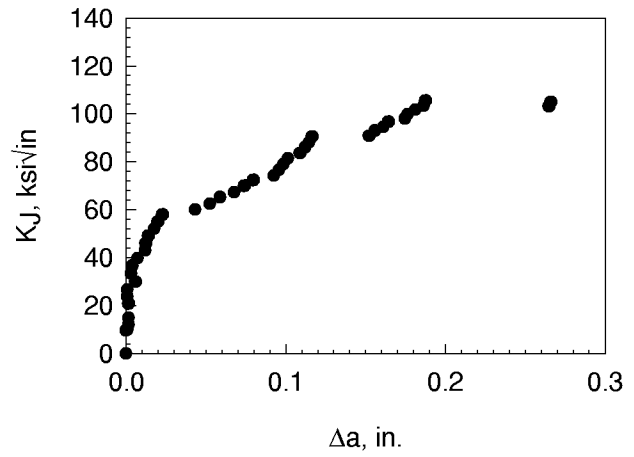
(a) 0° (A) orientation



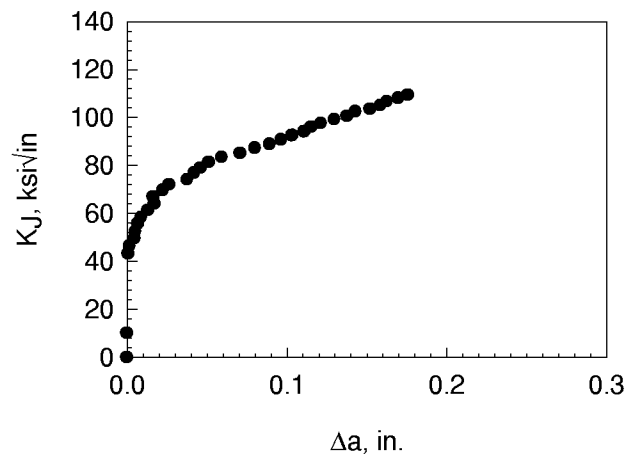
(b) 45° orientation



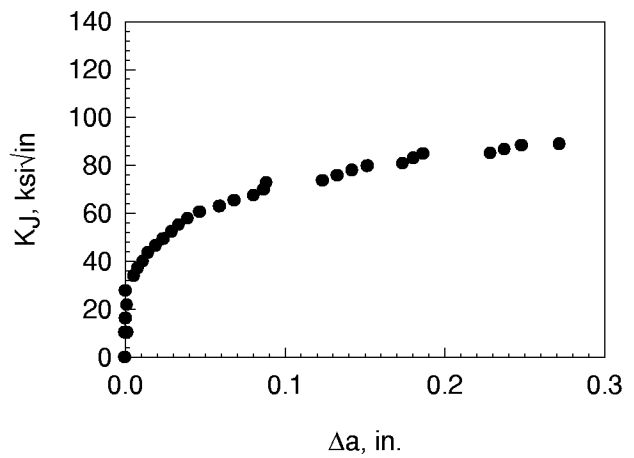
(c) 90° (C) orientation



(d) A-C orientation



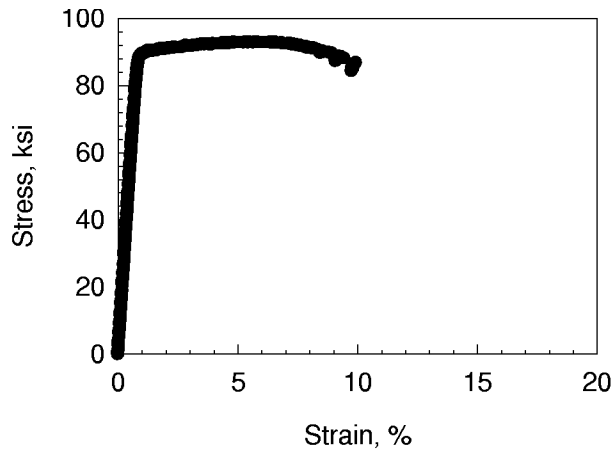
(e) 45-45 orientation



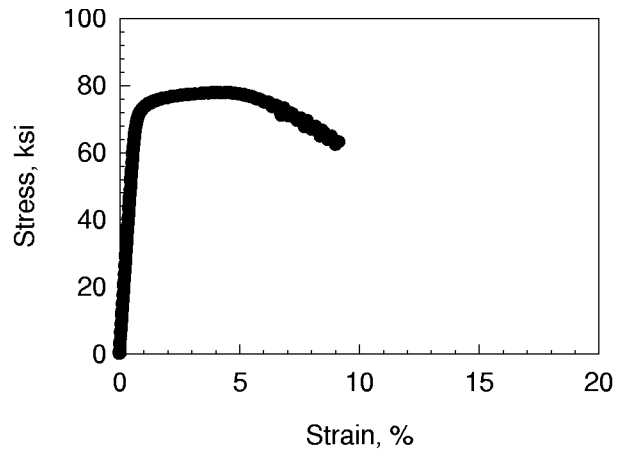
(f) C-A orientation

Figure A1. Mechanical behavior of 2195 Skin. Stress-strain curves and K-R curves for various orientations.

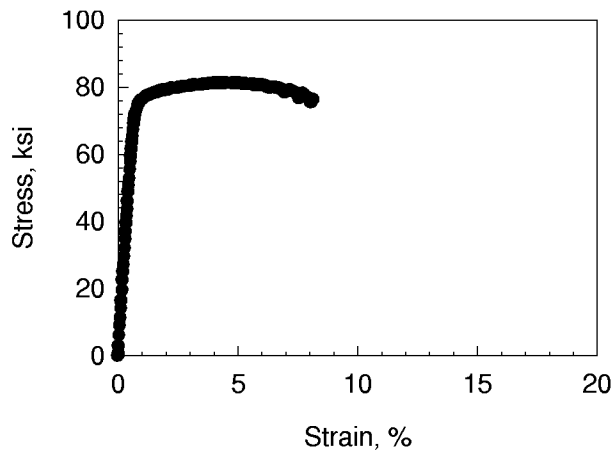




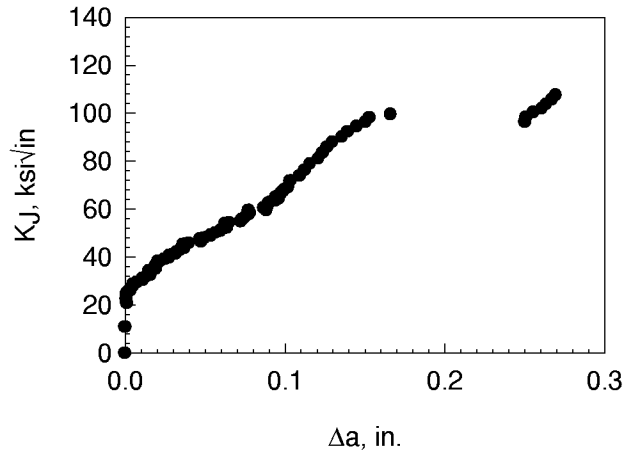
(a) 0° (A) orientation



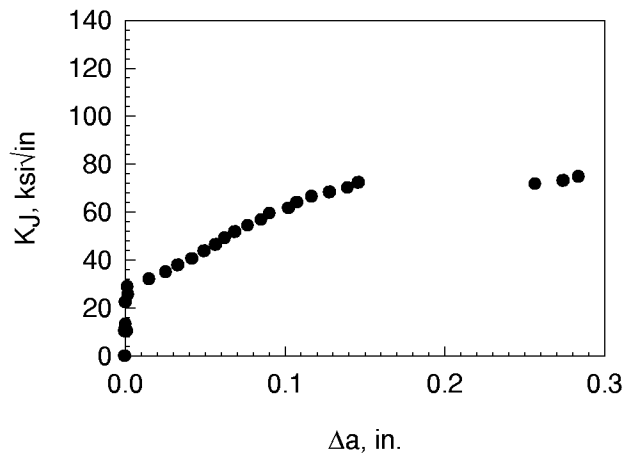
(b) 45° orientation



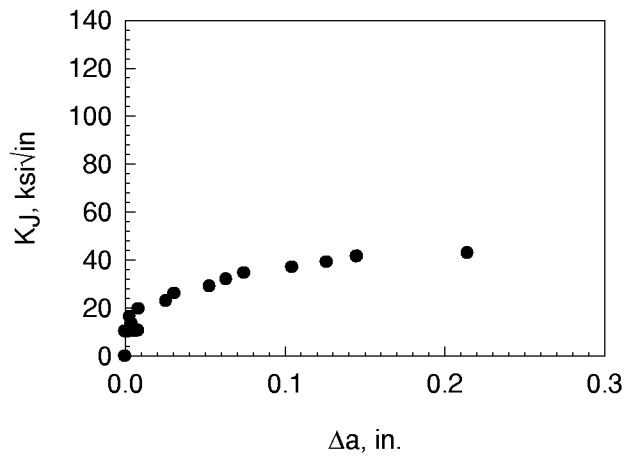
(c) 90° (C) orientation



(d) A-C orientation

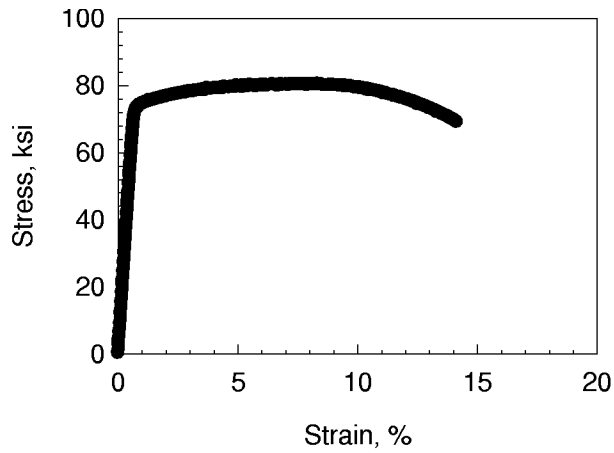


(e) 45-45 orientation

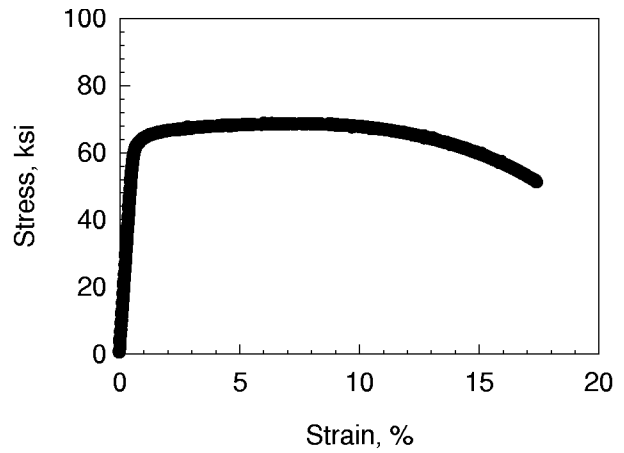


(f) C-A orientation

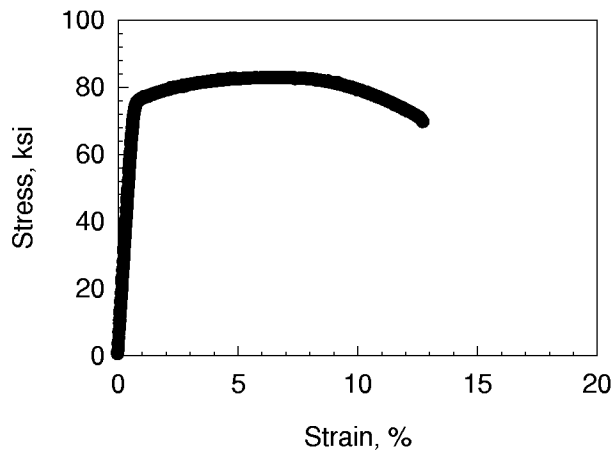
Figure A2. Mechanical behavior of 2195 Base. Stress-strain curves and K-R curves for various orientations.



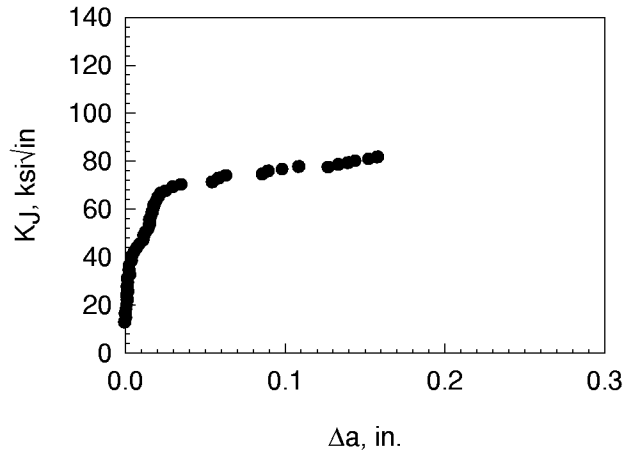
(a) 0° (A) orientation



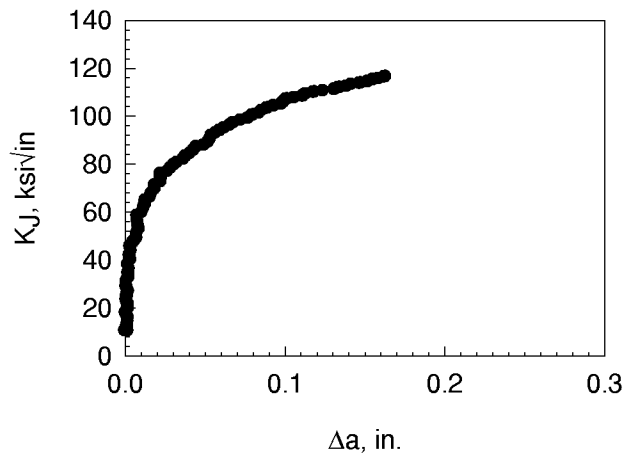
(b) 45° orientation



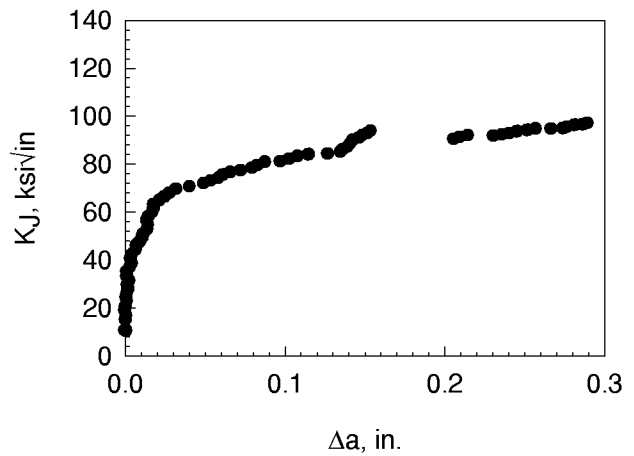
(c) 90° (C) orientation



(d) A-C orientation

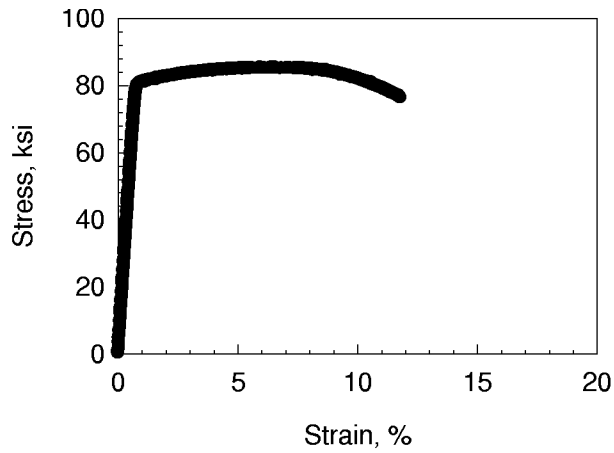


(e) 45-45 orientation

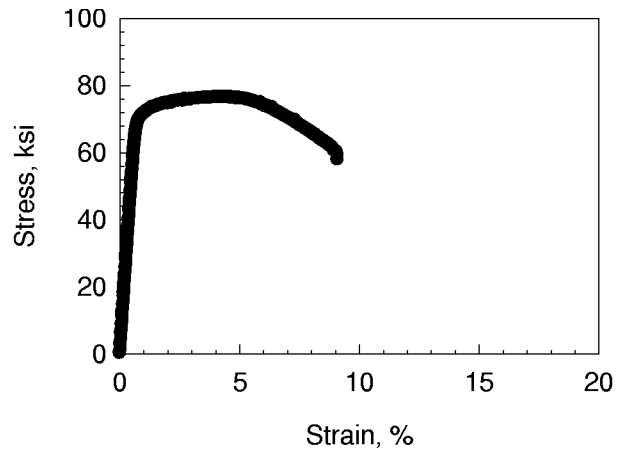


(f) C-A orientation

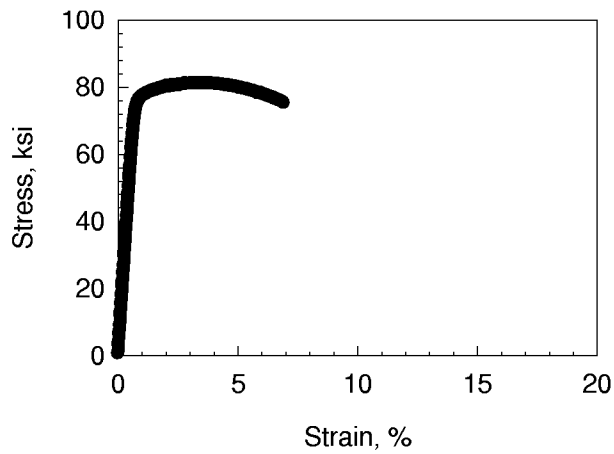
Figure A3. Mechanical behavior of 2098 Skin. Stress-strain curves and K-R curves for various orientations.



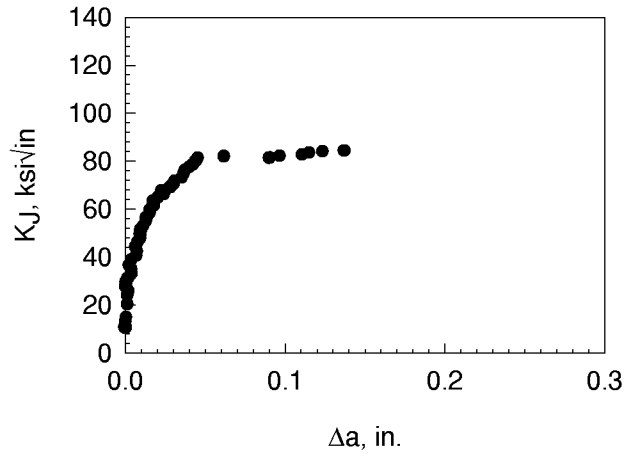
(a) 0° (A) orientation



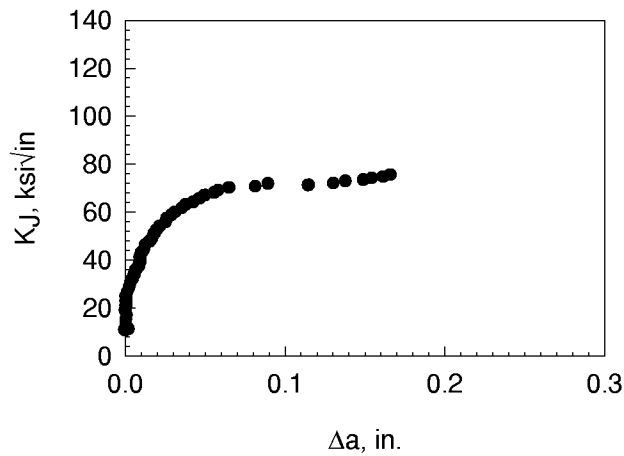
(b) 45° orientation



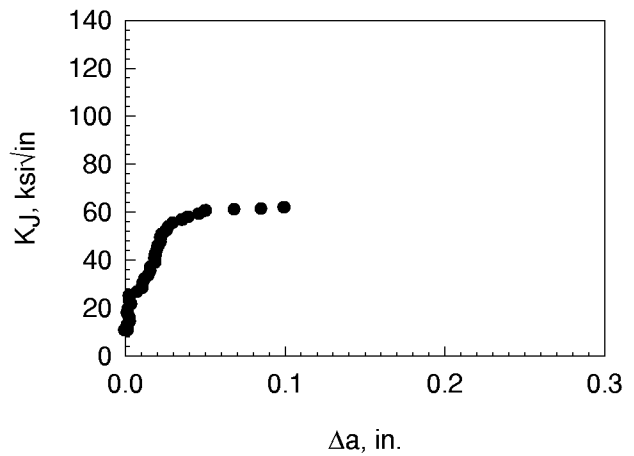
(c) 90° (C) orientation



(d) A-C orientation

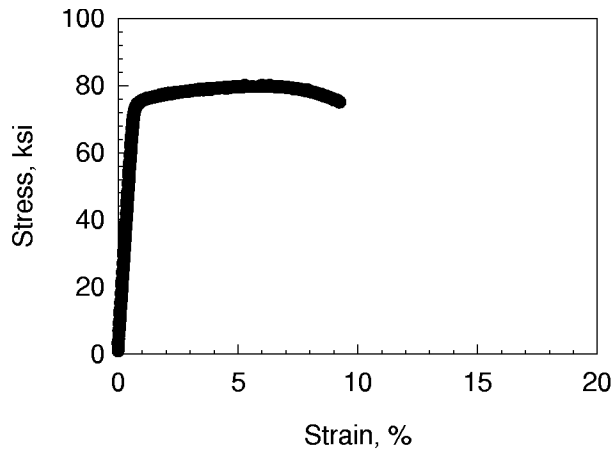


(e) 45-45 orientation

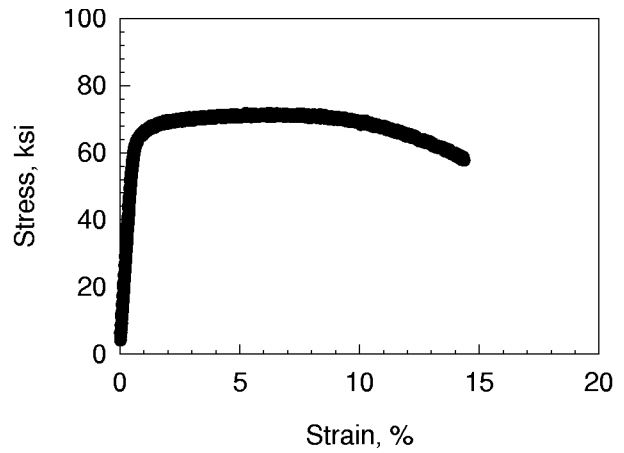


(f) C-A orientation

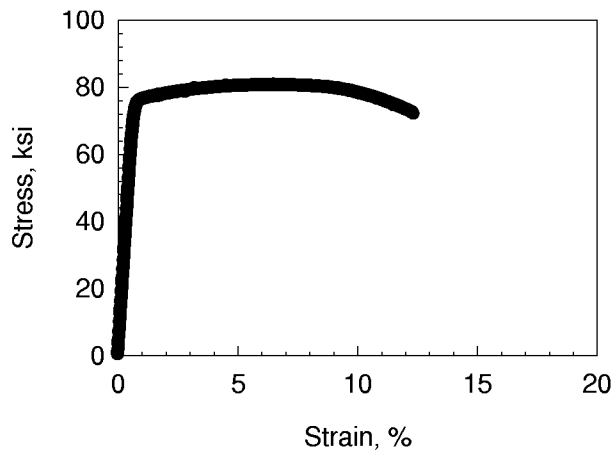
Figure A4. Mechanical behavior of 2098 Base. Stress-strain curves and K-R curves for various orientations.



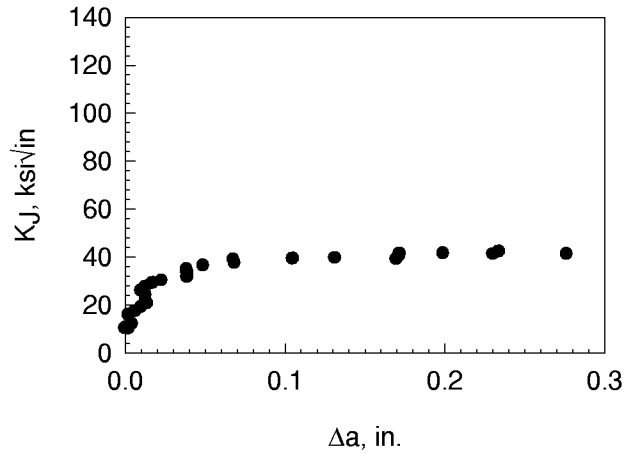
(a) 0° (A) orientation



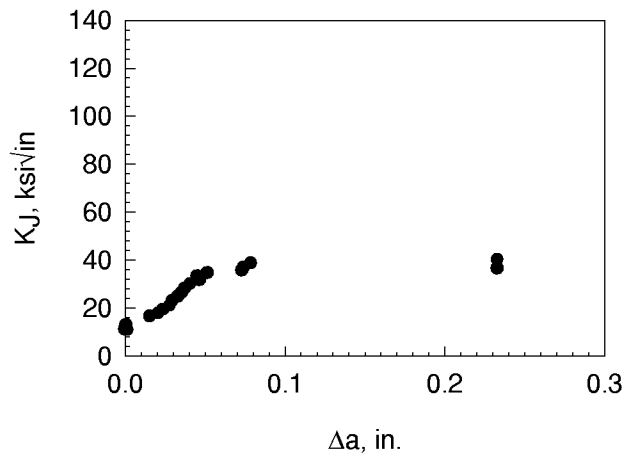
(b) 45° orientation



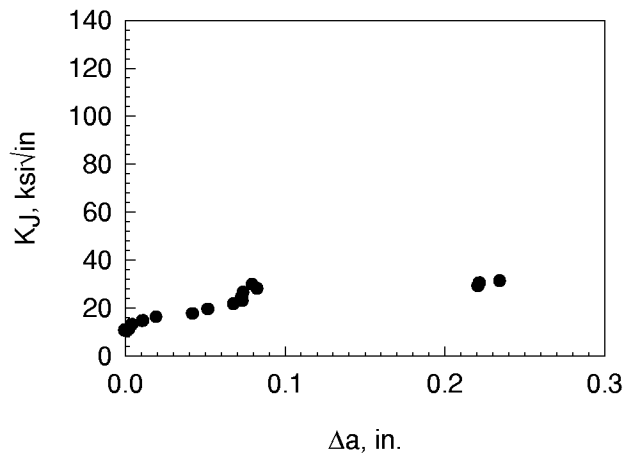
(c) 90° (C) orientation



(d) A-C orientation

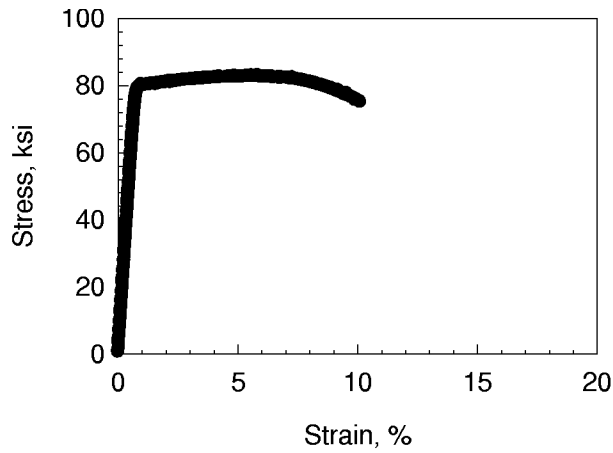


(e) 45-45 orientation

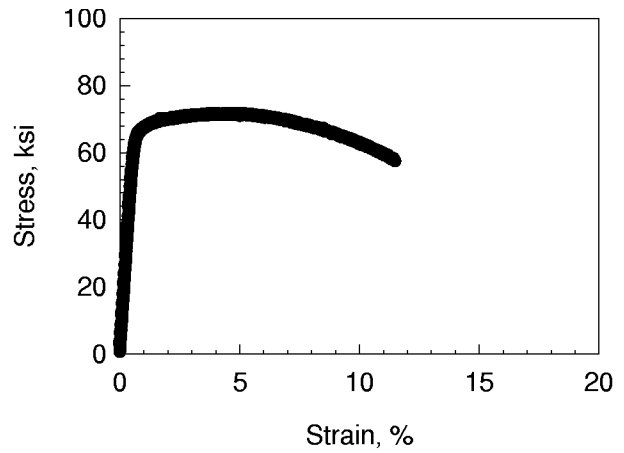


(f) C-A orientation

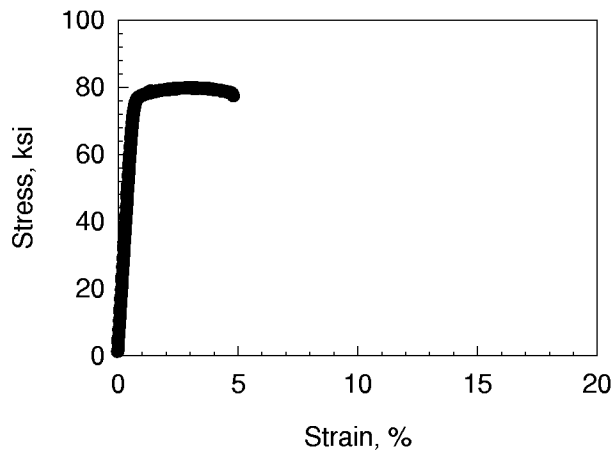
Figure A5. Mechanical behavior of 2096 Skin. Stress-strain curves and K-R curves for various orientations.



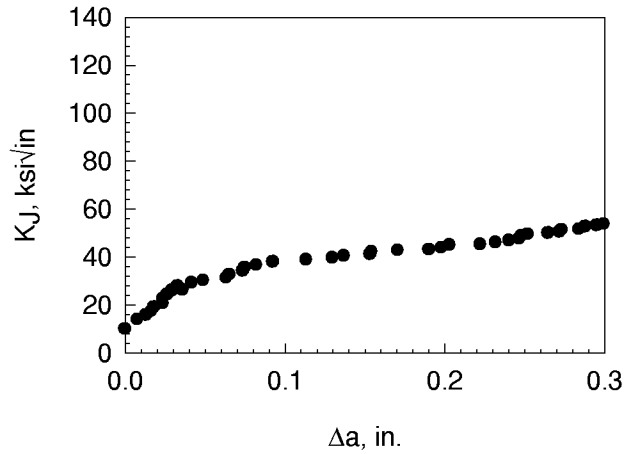
(a) 0° (A) orientation



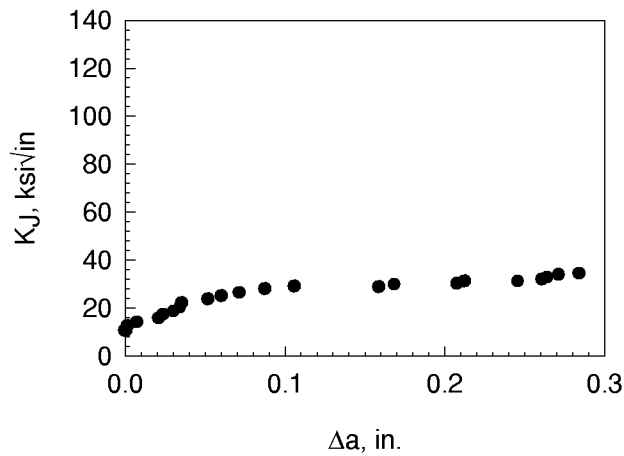
(b) 45° orientation



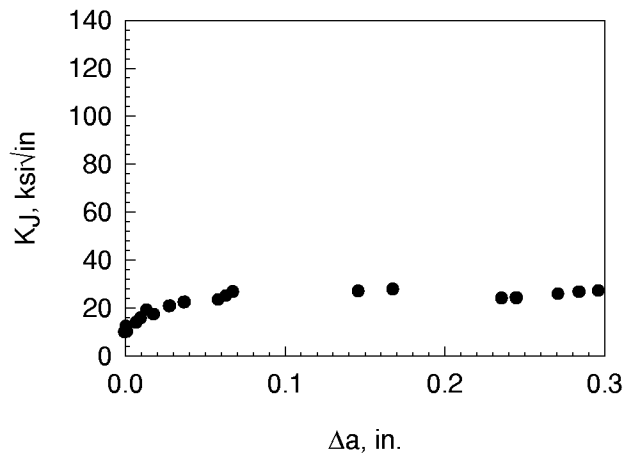
(c) 90° (C) orientation



(d) A-C orientation



(e) 45-45 orientation



(f) C-A orientation

Figure A6. Mechanical behavior of 2096 Base. Stress-strain curves and K-R curves for various orientations.

<b>REPORT DOCUMENTATION PAGE</b>			Form Approved OMB No. 0704-0188	
Public reporting burden for this collection of information is estimated to average 1 hour per response, including the time for reviewing instructions, searching existing data sources, gathering and maintaining the data needed, and completing and reviewing the collection of information. Send comments regarding this burden estimate or any other aspect of this collection of information, including suggestions for reducing this burden, to Washington Headquarters Services, Directorate for Information Operations and Reports, 1215 Jefferson Davis Highway, Suite 1204, Arlington, VA 22202-4302, and to the Office of Management and Budget, Paperwork Reduction Project (0704-0188), Washington, DC 20503.				
<b>1. AGENCY USE ONLY</b> (Leave blank)		<b>2. REPORT DATE</b> April 2001		<b>3. REPORT TYPE AND DATES COVERED</b> Technical Publication
<b>4. TITLE AND SUBTITLE</b> Structure-Property Correlations in Al-Li Alloy Integrally Stiffened Extrusions			<b>5. FUNDING NUMBERS</b>  WU 706-63-51-01	
<b>6. AUTHOR(S)</b> Stephen J. Hales and Robert A. Hafley				
<b>7. PERFORMING ORGANIZATION NAME(S) AND ADDRESS(ES)</b>  NASA Langley Research Center Hampton, VA 23681-2199			<b>8. PERFORMING ORGANIZATION REPORT NUMBER</b>  L-18066	
<b>9. SPONSORING/MONITORING AGENCY NAME(S) AND ADDRESS(ES)</b>  National Aeronautics and Space Administration Washington, DC 20546-0001			<b>10. SPONSORING/MONITORING AGENCY REPORT NUMBER</b>  NASA/TP-2001-210839	
<b>11. SUPPLEMENTARY NOTES</b>				
<b>12a. DISTRIBUTION/AVAILABILITY STATEMENT</b>  Unclassified-Unlimited Subject Category 26      Distribution: Standard Availability: NASA CASI (301) 621-0390			<b>12b. DISTRIBUTION CODE</b>	
<b>13. ABSTRACT</b> (Maximum 200 words) The objective of this investigation was to establish the relationship between mechanical property anisotropy, microstructure and crystallographic texture in integrally 'T'-stiffened extruded panels fabricated from the Al-Li alloys 2195, 2098 and 2096. In-plane properties were measured as a function of orientation at two locations in the panels, namely mid-way between (Skin), and directly beneath (Base), the integral 'T' stiffeners. The 2195 extrusion exhibited the best combination of strength and toughness, but was the most anisotropic. The 2098 extrusion exhibited lower strength and comparable toughness, but was more isotropic than 2195. The 2096 extrusion exhibited the lowest strength and poor toughness, but was the most isotropic. All three alloys exhibited highly elongated grain structures and similar location-dependent variations in grain morphology. The textural characteristics comprised a $\beta + <100>$ fiber texture, similar to rolled product, in the Skin regions and a $<111> + <100>$ fiber texture, comparable to axisymmetric extruded product, in the Base regions. In an attempt to quantitatively correlate texture with yield strength anisotropy, the original 'full constraint' Taylor model and a variant of the 'relaxed constraint' model, explored by Wert et al., were applied to the data. A comparison of the results revealed that the Wert model was consistently more accurate than the Taylor model.				
<b>14. SUBJECT TERMS</b> Aluminum-Lithium Alloys; Extrusions; Texture; Mechanical Properties; ODF; Taylor Factor; Relaxed Constraints Modeling			<b>15. NUMBER OF PAGES</b> 54	
			<b>16. PRICE CODE</b> A04	
<b>17. SECURITY CLASSIFICATION OF REPORT</b> Unclassified	<b>18. SECURITY CLASSIFICATION OF THIS PAGE</b> Unclassified	<b>19. SECURITY CLASSIFICATION OF ABSTRACT</b> Unclassified	<b>20. LIMITATION OF ABSTRACT</b> UL	